

On the dynamics of magnetoviscous warped discs around compact objects

Arthur G. Suvorov^{1,2*} and Kostas Glampedakis^{3,1†}

¹ Theoretical Astrophysics, Eberhard Karls University of Tübingen, Tübingen, D-72076, Germany

² Departament de Física, Universitat d'Alacant, Ap. Correus 99, E-03080 Alacant, Spain

³ Departamento de Física, Universidad de Murcia, Murcia, E-30100, Spain

Accepted ?. Received ?; in original form ?

ABSTRACT

Accretion discs that are tilted with respect to their compact hosts can warp out-of-plane through general relativistic frame-dragging. Warp influences disc dynamics in ways that have been studied extensively, especially as regards instabilities that might lead to rapid angular-momentum cancellation between neighbouring rings of fluid and mass infall. We provide a review of warped-disc phenomena here, revisiting key hydrodynamical assumptions that impact calculations of the shear viscosity controlling instability thresholds. Relativistic effects at the level of gas-parcel orbits are included, as are external Lorentz forces applied by the compact primary's magnetic field. Semi-analytic analysis reveals that intense magnetic fields can bring about new branches of warp modes and avoided crossings that significantly reduce the perpendicular viscosity at sub-Eddington accretion rates. Critical strengths required for misaligned torques to tear a thin disc may thus relax for systems like neutron star X-ray binaries or radio-loud active galactic nuclei.

Key words: Accretion discs, instabilities, magnetic fields, stars: neutron

1 INTRODUCTION

Accretion discs commonly encircle compact objects in astrophysical environments. The rate at which energy and angular momentum are transported in these systems depends on a number of factors, such as the orbital dynamics, optical depth, and thermodynamic equation of state (Frank, King & Raine 1992). Arguably, though, the most critical factor is viscosity: it is ultimately through dissipative processes that matter is able to accumulate onto the host's surface or, in the case of a black hole, fall through the horizon.

The benchmark model for accretion dynamics remains, in many respects, that pioneered by Shakura & Sunyaev (1973). The framework famously comes with an isotropic viscosity parameter, α , meaning that horizontal and vertical shears are damped at the same rate. However, because of the generally-small aspect ratio of astrophysical discs, this implies that the shear viscosity coefficients in orthogonal directions may not only be unequal but differ by orders of magnitude (Papaloizou & Pringle 1983; Ogilvie 1999; Lodato & Pringle 2007). Quantifying their relative size is central to mapping out onset criteria for magnetohydrodynamic (MHD) or other instabilities, often invoked to explain observed episodes of enhanced accretion (e.g., Balbus & Hawley 1998; Dubus, Hameury & Lasota 2001; Nixon 2015; Doğan et al. 2018; Raj & Nixon 2021).

Due to some combination of general relativistic (GR) effects (Bardeen & Petterson 1975), tidal forces (Papaloizou & Terquem 1995), gaseous lifting (Montgomery & Martin 2010), or irradiation (Pringle 1996), the disc may be off-centred relative to the equator of the primary. Tilt opens new possibilities for instability as, if the host also rotates rapidly, Lense-Thirring (LT) torques act on parcels of disc fluid in a directed manner such that they *warp* out-of-plane. Numerical (e.g., Raj, Nixon & Doğan 2021) and observational (e.g., Herrnstein, Greenhill & Moran 1996) evidence indicates that, for low enough α , warp modes may overwhelm restorative viscous forces in the disc. As described by Nixon et al. (2012) and others, it may thus *tear* into a number of precessing rings at certain characteristic radii determined by torque balance. As these rings collide and lose angular momentum, large and quasi-periodic mass deposits are made. To accurately assess whether tearing can explain observational puzzles – such as the rapid growth of black holes in the early universe (De Luca et al. 2025) or outbursts in low-mass X-ray binaries (LMXBs; Heinke et al. 2025) – one should include as many physical ingredients as possible when estimating viscosity coefficients.

In this paper, we add an extra layer of realism to the calculation by accounting for (i) GR adjustments to the epicyclic frequencies of gas parcels, and (ii) magnetic fields sourced by the primary. Aside from providing a critical review of the warped-disc literature – which can be difficult to navigate owing to swathes of notation and approximation – we find that external Lorentz forces can significantly change the nature of

* a.suvorov@uni-tuebingen.de

† kostas@um.es

warp eigenmodes (see also [Paris & Ogilvie 2018](#)). This impacts the horizontal-to-vertical viscosity relationship in ways we explore semi-analytically. Indeed, while GRMHD simulations have been carried out to examine instability thresholds, with the aim of determining where tearing may occur and how the system responds, they cannot reliably explore the whole parameter space due to computational expense (see [Fragile & Liska 2025](#), for a recent review). By using a hybrid analytic-plus-numerical approach, we hope to get a broader overview of how each piece of physics impacts warped-disc dynamics.

This paper is organised as follows. The thin-disc structure equations are reviewed in Section 2, including how warps may be accounted for (Sec. 2.2), GR aspects related to realignment through the Bardeen-Petterson effect (Sec. 2.3), and tearing theory (Sec. 2.4). A local analysis of how fluid parcels within a warped disc may behave is presented in Section 3, comparing the Newtonian and GR regimes (Sec. 3.2), expectations for the viscous shear coefficients (Sec. 3.3), and hydrodynamical instabilities as a function thereof (Sec. 3.4). The main results concerning the inclusion magnetic fields are given in Section 4, where we systematically revisit all previous aspects, notably discussing mode bifurcations and avoided crossing phenomena (Sec. 4.2). The impact of GR and magnetic effects on expectations for astrophysical systems is examined in Section 5 for a variety of systems, including LMXBs (Sec. 5.3). Some closing discussion is offered in Section 6.

2 WARPED DISC PHENOMENOLOGY

We begin by reviewing some of the basic principles associated with warped disks as found in the literature. More careful analyses at the level of local fluid displacement (Sections 3 and 4), where the physical principles are explored mathematically, are deferred for now in favour of a more pedagogical treatment.

2.1 Basic equations and relations of disc structure

Without warp, the system is assumed to be a standard [Shakura & Sunyaev \(1973\)](#) thin disc with thickness $H \ll r$ and viscosity parameter $\alpha < 1$. We use standard notation for the disc parameters for coordinate radius r : $\Omega(r)$ is the angular velocity profile (typically assumed to be Keplerian), Σ is the surface density, $\nu = \eta/\rho$ is the dynamical viscosity coefficient, and c_s is the speed of sound. Useful textbook relations between them are given below ([Frank, King & Raine 1992](#)):

$$\Sigma = \rho H, \quad \dot{M} \approx \nu \Sigma, \quad c_s \approx H \Omega = \frac{H}{r} v_\varphi, \quad \nu \approx \alpha H c_s, \quad (1)$$

where $v_\varphi = r \Omega$ is the rotational (azimuthal) speed. From these expressions we can obtain the density profile of a Keplerian disc

$$\rho(r) = \frac{\dot{M}}{3\pi\alpha} \left(\frac{H}{r} \right)^{-3} (GMr^3)^{-1/2}. \quad (2)$$

Unit vectors are denoted by a ‘hat’ while a prime denotes a derivative with respect to the function’s argument. We use \mathbf{N} and \mathbf{T} for the total torque and the torque exerted per unit mass, respectively. The disc’s angular momentum per unit area is denoted by $\boldsymbol{\ell}$; for a thin equatorial disc this is

$$\boldsymbol{\ell} = \Sigma r^2 \Omega \hat{\mathbf{z}}. \quad (3)$$

When convenient, we use dimensionless parameters for the radius, $\bar{r} = rc^2/GM$, and the central body’s spin parameter, $q = cJ/GM^2$ (M and J denote the primary’s mass and angular momentum) and/or relativistic units $G = c = 1$. It is also convenient to introduce the Eddington accretion rate

$$\dot{M}_{\text{edd}} \approx 1.5 \times 10^{-8} (R/10 \text{ km}) M_\odot \text{ yr}^{-1}, \quad (4)$$

to set units for \dot{M} , where R denotes the radius of the compact object (set to the ‘canonical’ neutron star radius with a bit of foresight). The structure equations predict a nearly uniform disc thickness ratio which we show here for parameters normalised to those of an accreting neutron star (and omitting a small relativistic factor):

$$\begin{aligned} \frac{H}{r} \approx 2 \times 10^{-3} \left(\frac{\alpha}{0.1} \right)^{-1/10} \left(\frac{\dot{M}}{10^{-5} \dot{M}_{\text{edd}}} \right)^{3/20} \left(\frac{R}{10 \text{ km}} \right)^{11/40} \\ \times \left(\frac{M}{1.4 M_\odot} \right)^{-3/8} \left(\frac{r}{R} \right)^{1/8}. \end{aligned} \quad (5)$$

When convenient, we will use the shorthand notation $H_0 = H/r$ for this ratio and keep H_0 as effectively free to explore a wider range of dynamical interactions.

2.2 Warped disc geometry

In the case of a warped disc it is useful to introduce the unit tilt vector, $\hat{\boldsymbol{\ell}} = \boldsymbol{\ell}/\ell$. By its definition this is orthogonal to the local disc/orbital plane (e.g. for the standard flat thin disc model we would have $\hat{\boldsymbol{\ell}} = \hat{\mathbf{z}} = \text{const.}$). In general, this vector is a function $\hat{\boldsymbol{\ell}}(t, \mathbf{x})$ of the fixed global coordinates. However, we can use ‘warp-adapted’ coordinates (see, e.g., [Papaloizou & Pringle 1983](#), henceforth PP83) so that each disc ring at distance r from the center is axisymmetric and, as a result, $\hat{\boldsymbol{\ell}} = \hat{\boldsymbol{\ell}}(t, r)$, where r can be a spherical or a cylindrical radius. These adapted coordinates emerge ‘naturally’ by considering the local exchange of angular momentum between adjacent rings in the warped disc ([Ogilvie 1999](#)).

With the help of the tilt vector, we can define the vectorial warp as

$$\psi(t, r) = r \frac{\partial \hat{\boldsymbol{\ell}}}{\partial r}. \quad (6)$$

Roughly speaking, the warp parameter encodes the radial variability of the disc’s tilt. Throughout most of this work we use a ‘small-warp’ approximation, amounting to $|\psi| \ll 1$, to explore perturbative corrections to the disc structure equations; see, however, [Ogilvie \(1999\)](#) for a discussion on the validity of this approach and its comparison with the full Navier-Stokes system for warped discs.

2.3 Bardeen-Petterson alignment

One aspect of relevance to warp considerations is the [Bardeen & Petterson \(1975\)](#) (BP) effect: it has been argued that the inner region of a disk should gradually align with the equatorial plane of the compact primary (though cf. [Kumar & Pringle 1985; Scheuer & Feiler 1996](#)). The effect stems from the assumption that perturbations between neighbouring rings of gas, in a tilted disc subject to radially-dependent (i.e. LT) torques, propagate in a diffusive regime. Such diffusive processes cause any angular-momentum misalignments to be smoothed out to some transition radius (r_{BP}) set by the

competition between viscosity and differential precession. Beyond this critical radius, LT torques become small and tilt is set instead by the direction of gas infall, leading to the picture of a midplane-oriented disc with thickened ‘arms’ extending at some angle; see, e.g., Fig. 1 in [Fragile, Mathews & Wilson \(2001\)](#). If the BP effect operates, one would not expect any significant warp in the inner regions of the disc owing to its alignment and hence the system may be in a (quasi-)equilibrium state.

Such an application is subtle however. PP83 subsequently argued that even if the disc viscosity is assumed isotropic, damping timescales in the vertical and radial directions are not equal owing to the small aspect ratio of the disc (such a relationship is quantified in Sec. 3). This, together with the fact that disturbances may instead propagate in a wave-like regime for some microphysical combinations (see below), implies that the BP effect may not occur and instead more catastrophic phenomena in the form of *tearing* can take place.

2.4 Fragmentation and tearing

Although a mixed scheme is likely to apply in reality, the perturbation dynamics of a warped disc are typically discussed in two distinct regimes. These correspond to either $\alpha \ll H/r$, where viscous damping is weak enough for modes to effectively propagate in a wavelike manner, or $\alpha \gg H/r$, where modes may be damped before completing full oscillations (a diffusive regime where the BP effect may operate; see [Pringle 1992](#); [Nixon et al. 2012](#)). It is typically only in the wavelike case that stress may build up in such a way that a disc may be locally overwhelmed and ‘break’ in some sense.

Following [Raj, Nixon & Doğan \(2021\)](#), the word *break* used above simply conveys that there exists a mode, scaling as $\propto e^{i\omega t}$, such that the complex eigenfrequency ω has a negative imaginary component. This implies a runaway instability where the mode amplitude grows, meaning that the perturbed warp, $\delta\psi$, may become large enough to snap the disc at some position. The word *tearing*, by contrast, is typically applied in the context where external (i.e., primary or companion sourced) torques act on the disc and are necessary for inducing such a break. They convey the same physics therefore, though it is the latter which is of primary relevance since an intrinsically-unstable disc is unlikely to persist over astrophysical timescales. In the case of primary-sourced rotation, [Nixon & King \(2012\)](#) argue that viscous torques cannot override the LT torque if the warp exceeds a critical amplitude, leading to fragmentations into precessing rings within the disc mid-plane. Precessional grinding between these rings leads to the eventual loss of their angular momentum such that the gas then falls quasi-radially onto the host object, increasing \dot{M} relative to a quiescent state ([Nixon et al. 2012](#)). An illustration of how warp and precessional grinding may manifest within a tilted disc is provided in Figure 1.

Either way, such an analysis – revisited via a hydrodynamic description in Sec. 3.4 – only indicates the physical parameters under which a break may occur. It does not, however, identify the radial position, which is important to quantify if one wishes to estimate the amount of mass that may be contained in a broken region that may eventually contribute to a brightening episode (see Sec. 5).

To estimate the tearing radius, r_t , we work with torques per unit mass and closely follow [Tremaine & Davis \(2014\)](#).

To leading post-Newtonian order, the LT torque formula is

$$T_{\text{LT}} = \frac{2c^2 q}{\bar{r}^{5/2}} (\hat{\mathbf{J}} \times \hat{\boldsymbol{\ell}}) \Rightarrow T_{\text{LT}} = \frac{2c^2 q}{\bar{r}^{5/2}} \sin \beta, \quad (7)$$

where we have introduced the tilt angle β . Note that this torque is always orthogonal to the central body’s spin axis, $\mathbf{T}_{\text{LT}} \cdot \hat{\mathbf{z}} = 0$. The tearing action of \mathbf{T}_{LT} is counteracted by viscous forces arising from the shearing motion in a direction orthogonal to the disc plane. As a consequence, we need to introduce a ‘perpendicular’ viscosity coefficient ν_{\perp} which may be distinct from the more familiar ‘equatorial’ viscosity coefficient ν of the standard α -disc¹. Using a similar α -parametrisation for this perpendicular viscous torque to the standard [Shakura & Sunyaev \(1973\)](#) one, we have

$$T_{\perp} \sim |\psi| \nu_{\perp} \Omega \sim |\psi| \alpha_{\perp} H^2 \Omega^2 \approx |\psi| \alpha_{\perp} \left(\frac{H}{r} \right)^2 \frac{c^2}{\bar{r}}. \quad (8)$$

Then, the criterion for disc tearing becomes

$$\frac{T_{\text{LT}}}{T_{\perp}} \gtrsim 1 \Rightarrow \bar{r}_t \lesssim \left(\sin \beta \frac{q}{\alpha_{\perp} |\psi|} \right)^{2/3} \left(\frac{H}{r} \right)^{-4/3}. \quad (9)$$

This result displays the expected dependence on the tilt angle β and the central body’s spin q . However, the viscosity dependence is a more subtle issue because of the ‘anomalous’ relation $\alpha_{\perp}(\alpha)$ which may cause r_t to *grow* with α ([Papaloizou & Pringle 1983](#); [Kumar & Pringle 1985](#)). In fact, one of the main goals of this work to revisit this relationship and see how it changes in the presence of GR effects and central body-hosted magnetic fields.

It is important to recognise that the radii r_{BP} and r_t essentially represent the same effect in different parts of the parameter space. For example, the former radius can describe the case of an aligned disc following the suppression of the LT effect by viscosity (assuming the tilt radius was small to begin with). The latter radius would represent the case where the LT force dominates over viscosity, leading to the formation of decoupled precessing rings. This dichotomy is exemplified in Fig. 11 of [Nealon, Price & Nixon \(2015\)](#): below (above) a critical tilt angle the disc BP-aligns (fragments into rings) under the competitive actions of viscosity and LT precession.

3 LOCAL FLUID-PARCEL ANALYSIS

3.1 Equations of motion and their solutions

As mentioned earlier, a local analysis provides a relatively simple approach to modelling the dynamics of a warped disc with the possibility of including additional degrees of freedom like relativistic effects and an external magnetic field.

Following [Lodato & Pringle \(2007\)](#) (hereafter LP07), we model a disc fluid element as a test body of mass m subject to relativistic gravity and a viscous drag force. In addition we include a force induced by the disc warping; a local non-zero warp leads to a radial (locally equatorial) pressure gradient with magnitude (see also Fig. 1)

$$\partial_r p \sim \partial_z p \psi \sim \frac{p}{H} \psi, \quad (10)$$

¹ This point becomes apparent if we recall that the viscous torque in a thin Keplerian disc is $\mathbf{N}_{\text{visc}}(r) \approx 2\pi\nu\Sigma r^3 \Omega' \hat{\mathbf{z}}$ ([Frank, King & Raine 1992](#)), which is orthogonal to the LT torque.

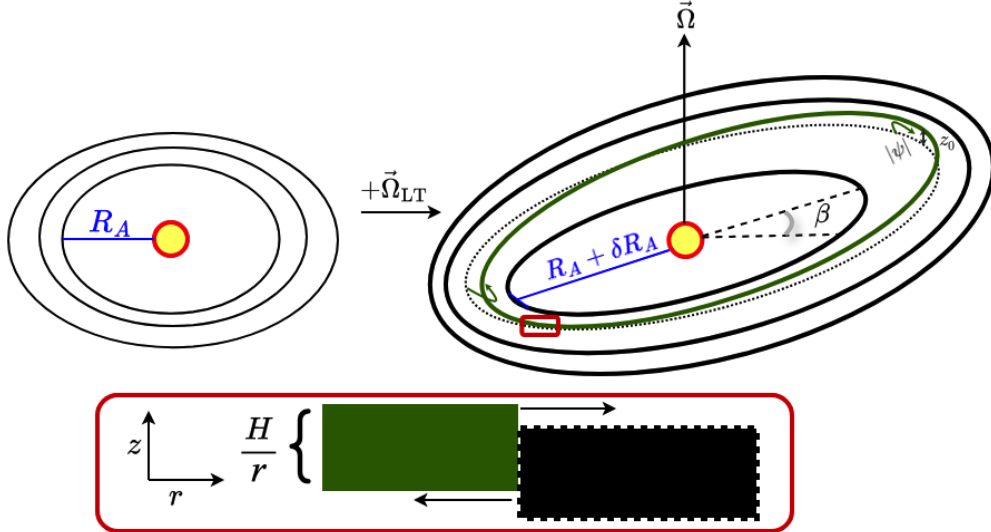


Figure 1. Schematic of a tilted accretion disc around a compact object. If sufficiently magnetised, truncation of the disc occurs at the Alfvén radius, R_A , where magnetic pressure balances the ram pressure of circulating material (left; see Sec. 4.2 for a definition). In cases of dynamical capture, young systems, or where the BP effect is not at work, there is no further expectation of any existing disc-object symmetry: the inner region(s) may be angled (β) with respect to the mid-plane of the compact primary as rotation and Lense-Thirring torques (Ω_{LT}) are ‘switched on’ (right). A differential precession is thus exerted on radially-neighbouring parcels of fluid which drives a warp ($|\psi|$) which depends on the amplitude of disturbances (z_0 ; see Sec. 3). Pressure gradients between neighbouring ‘rings’, which vary as a function of polar angles, result from this warp. This effect is illustrated in the red-box inset. Balancing the energy-dissipation rates between shear motions in two orthogonal directions leads to estimations of the vertical and radial dissipation timescales (see also section 4.1 in Lodato & Pringle (2007), from which parts of this figure are adapted).

where it is assumed that the warp angle $\psi \sim dz/dr$ is small. The (radial) acceleration associated with this force is

$$\frac{1}{\rho} \partial_r p \sim \frac{c_s^2}{H} \psi \sim H \Omega^2 \psi. \quad (11)$$

For the viscous force we use the simple Stokes formula, allowing for an anisotropic drag coefficient (see discussion below on this point)

$$\mathbf{f}_{\text{visc}} = -m \lambda_i \mathbf{v} \quad (i = \{x, y, z\}). \quad (12)$$

The validity of this formula hinges on a laminar and sub-sonic flow, which need not be satisfied throughout the disc. Nevertheless, it provides a reasonable approximation for our purposes and is standard in studies of linear stability; see Section 4 of Brandenburg (2008) for a discussion on different regimes.

The above forces are of hydrodynamical origin and are supposed to act as perturbations to the body’s geodesic motion. For the latter motion we can use exact equations if the central body is a Kerr black hole or a slow-rotation limit of the same equations if the central body is a neutron star or some other material system. These textbook equations are shown in Appendix A. We apply them to the case of a fluid element perturbed away from a circular equatorial orbit, i.e.

$$r(t) = r_0 + \delta r(t), \quad \theta(t) = \frac{\pi}{2} + \delta \theta(t), \quad (13)$$

where $\{t, r, \theta\}$ now stand for the standard Boyer-Lindquist coordinates of the Kerr spacetime (ignoring the azimuth). As shown in Appendix A, the motion is described by the two decoupled harmonic oscillators

$$\frac{d^2 \delta r}{dt^2} + \Omega_r^2 \delta r = 0, \quad \frac{d^2 \delta \theta}{dt^2} + \Omega_\theta^2 \delta \theta = 0, \quad (14)$$

where we henceforth use an overhead dot to denote (coordinate) time differentiation. Adopting for the moment geometric units $G = c = 1$, we define the dimensionless parameters $q = a/M$ and $x = M/r_0 = (M\Omega_0)^{2/3}$, where $\Omega_0 = \Omega(r_0)$. We can subsequently write the epicyclic orbital frequencies Ω_r, Ω_θ in terms of these parameters as

$$\Omega_r^2 = \frac{x^3 - 6x^4 + 8qx^{9/2} - 3q^2 x^5}{M^2(1 + qx^{3/2})^2}, \quad (15)$$

$$\Omega_\theta^2 = \frac{x^3 - 4qx^{9/2} + 3q^2 x^5}{M^2(1 + qx^{3/2})^2}. \quad (16)$$

As mentioned, these expressions are ‘exact’ for orbits outside black holes but they need to be truncated to $\mathcal{O}(q)$ for accreting neutron stars as their exterior spacetime is not Kerr (see, e.g., Pappas 2017). In fact, if we want to amend (14) with the aforementioned hydrodynamical forces (i.e., expressions 11 and 12) we should interpret them as quasi-Newtonian equations [the error involved in doing this approximation is $\mathcal{O}(x)$ in the solutions $\delta r, \delta \theta$]. The resulting system reads

$$\ddot{\delta r} + \Omega_r^2 \delta r + \lambda \delta \dot{r} = H \Omega_0^2 \psi(t), \quad (17)$$

$$\ddot{\psi} + \Omega_\theta^2 \psi + \lambda_\perp \dot{\psi} = 0, \quad (18)$$

where we have replaced $\delta \theta \sim \psi$ and introduced the horizontal and perpendicular drag coefficients λ, λ_\perp . This system of equations generalises the analysis of LP07 by including relativistic orbital frequencies and a dissipative term in the warp’s equation of motion (see their Section 4.1).

The solution of the warp equation (18) (with an appropri-

ate choice of initial conditions) can be written as

$$\psi(t) = \psi_0 e^{-\lambda_\perp t/2} \sin \omega_\theta t, \quad (19)$$

where ψ_0 is a constant amplitude and $\omega_\theta = (\Omega_\theta^2 - \lambda_\perp^2/4)^{1/2}$. In the case of weak damping, $\lambda_\perp \ll \Omega_\theta$, we can approximate $\omega_\theta \approx \Omega_\theta \approx \Omega_0$, and the solution is oscillatory over an interval $t \sim 1/\lambda_\perp$. The opposite case of strong damping, $\lambda_\perp \gg \Omega_\theta$, is characterised by an imaginary $\omega_\theta = i(\lambda_\perp^2/4 - \Omega_\theta^2)^{1/2} = i\tilde{\omega}_\theta$ and the time evolution is a purely exponential decay with a late time profile $\psi \sim e^{(\tilde{\omega}_\theta - \lambda_\perp/2)t}$. These two limiting cases provide a link to the previous torque-based tearing radius calculation: weak (strong) damping is associated with a dominant LT (viscous) torque. A necessary condition for the disc to be driven to a tearing regime is that it should be allowed to oscillate perpendicularly (LT precession) over several orbital periods so that adjacent rings can develop a sufficiently large relative displacement.

Going back to the fluid parcel's radial equation of motion (17), we have the updated expression

$$\delta\ddot{r} + \Omega_r^2 \delta r + \lambda \delta\dot{r} = H\Omega_0^2 \psi_0 e^{-\lambda_\perp t/2} \sin \omega_\theta t. \quad (20)$$

Considering only the particular, warp-driven, solution of this equation, we find

$$\delta r(t) = \mathcal{A} e^{-\lambda_\perp t/2} \sin(\omega_\theta t + \phi), \quad (21)$$

where ϕ is a constant phase and

$$\mathcal{A} = \frac{H\psi_0\Omega_0^2}{\sqrt{\lambda_\perp^2\Omega_r^2 + \lambda^2\Omega_\theta^2} - \lambda\lambda_\perp(\Omega_r^2 + \Omega_\theta^2) + (\Omega_r^2 - \Omega_\theta^2)^2}. \quad (22)$$

The expression for the amplitude can be simplified by approximating $\Omega_{r,\theta} \approx \Omega_0$ in the *viscosity* terms,

$$\mathcal{A} \approx \frac{H\psi_0\Omega_0^2}{\sqrt{(\lambda_\perp - \lambda)^2\Omega_0^2 + (\Omega_r^2 - \Omega_\theta^2)^2}}. \quad (23)$$

We can employ a standard α -parametrisation for the damping rates, $\lambda = \alpha\Omega_0$ and $\lambda_\perp = \alpha_\perp\Omega_0$, to furthermore write

$$\mathcal{A} \approx \frac{H\psi_0}{\sqrt{(\alpha_\perp - \alpha)^2 + [(\Omega_r^2 - \Omega_\theta^2)/\Omega_0^2]^2}}. \quad (24)$$

The structure of this amplitude is quite revealing: an orbital resonance between the two epicyclic frequencies maximises the fluid parcel's radial displacement. The resonance is exact in the case of Newtonian gravity ($\Omega_r = \Omega_\theta$) but there is a small shift when GR corrections are included. We discuss these two regimes in the following section.

3.2 Newtonian versus relativistic regime

If we assume (as in LP07) a Newtonian gravitational field, so that $\Omega_r = \Omega_\theta = \Omega_0$ exactly, we find the following Newtonian oscillation amplitude

$$\mathcal{A} \approx \mathcal{A}_N = \frac{H\psi_0}{|\alpha_\perp - \alpha|}. \quad (25)$$

Having at our disposal the fully relativistic orbital frequencies (15) we can refine this Newtonian result by first expanding in the post-Newtonian parameter $x \ll 1$

$$\begin{aligned} \Omega_r^2 - \Omega_\theta^2 &= \frac{6x^4}{M^2} \left(\frac{1 - qx^{1/2}}{1 + qx^{3/2}} \right)^2 \\ &\approx \frac{1}{M^2} \left[6x^4 - 12qx^{9/2} + \mathcal{O}(q^2, x^5) \right]. \end{aligned} \quad (26)$$

We can then see that the above Newtonian approximation amounts to the condition

$$|\alpha_\perp - \alpha| \gg x. \quad (27)$$

(Normal human units can be restored with $x \rightarrow GM/r_0 c^2$.) In the same Newtonian regime, the radial velocity is

$$\delta v_r = \delta\dot{r} \approx \frac{H\Omega_0\psi_0}{|\alpha_\perp - \alpha|} \approx \frac{c_s\psi_0}{|\alpha_\perp - \alpha|}. \quad (28)$$

In the opposite limit, which we may call 'relativistic', we have

$$|\alpha_\perp - \alpha| \ll x, \quad (29)$$

leading to a viscosity-independent radial motion amplitude

$$\mathcal{A} \approx \mathcal{A}_{GR} = \frac{H\psi_0}{6x}. \quad (30)$$

The corresponding velocity amplitude is

$$\delta v_r \approx \frac{c_s\psi_0}{6x}. \quad (31)$$

We can see that

$$\frac{\mathcal{A}_{GR}}{\mathcal{A}_N} \approx \frac{|\alpha_\perp - \alpha|}{x}, \quad (32)$$

which means that the relativistic regime implies a suppressed radial displacement and velocity. This is not surprising given this regime's weaker resonance between the radial and vertical oscillation frequencies.

It is clear that the Newtonian regime is the suitable one for the greatest portion of an astrophysical accretion disc for 'canonical' values $\alpha \approx 0.1$ (excluding the fine-tuned situation $\alpha_\perp \approx \alpha$). The disc may extend down to the relativistic innermost stable orbit (at $x = 1/6 \approx 0.17$ for a non-spinning black hole) which means that the relativistic regime requires the alpha parameters be of order $\sim 10^{-2}$ or less. As we show in the following section the refined threshold for the relativistic regime turns out to be $\alpha \ll x^3$. There is, of course, nothing sacred about 'canonical' values $\alpha \approx 0.1$. Indeed, as we discuss in Section 5.1, the anticipated values of α in astrophysical systems may lie much below (or even much above!) the canonical value, suggesting that the relativistic regime could be physically relevant in some cases.

3.3 Relating the two viscosities

As discussed in LP07, the fact that the horizontal and vertical motions are interrelated (i.e. the horizontal shearing motion is driven by the disc's warp) implies a balance in the corresponding viscous dissipation rates. In terms of the fluid velocities in cylindrical coordinates (r, z) , we should have

$$\nu_\perp \langle (\partial_r \delta v_z)^2 \rangle = \nu \langle (\partial_z \delta v_r)^2 \rangle. \quad (33)$$

The angled brackets denote an averaging over many hydrodynamical timescales to wash out oscillatory motions. The vertical velocity is calculated as

$$\delta v_z \approx r_0 \dot{\psi} \approx r_0 \Omega_0 \psi_0 e^{-\lambda_\perp t/2} \cos \Omega_0 t, \quad (34)$$

and its r -derivative can be approximated as $\partial_r \delta v_z \approx \delta v_z / r_0$. For the z -derivative of the radial velocity we use the approximation²

$$\partial_z \delta v_r \approx \frac{\delta v_r}{H} \approx \frac{\mathcal{A}\Omega_0}{H} e^{-\lambda_\perp t/2} \cos(\Omega_0 t + \phi). \quad (35)$$

² This, as well as the previous approximation for ∂_r concerning expression (11), is oblivious to the sign of the actual derivative;

The time average of these derivatives in the weak viscosity regime ($\lambda_{\perp} \ll \Omega_0$) is found to be

$$\langle (\partial_r \delta v_z)^2 \rangle \approx \frac{1}{2} \psi_0^2 \Omega_0^2, \quad (36)$$

$$\langle (\partial_z \delta v_r)^2 \rangle \approx \frac{1}{2} \mathcal{A}^2 \Omega_0^2. \quad (37)$$

Inserting these in the balance equation (33) we obtain

$$\frac{\nu_{\perp}}{\nu} = \frac{\alpha_{\perp}}{\alpha} \approx \left(\frac{\mathcal{A}}{\psi_0 H} \right)^2. \quad (38)$$

Evaluating this in the Newtonian regime, $\mathcal{A} = \mathcal{A}_N$, via expression (25),

$$\frac{\alpha_{\perp}}{\alpha} \approx \frac{1}{(\alpha_{\perp} - \alpha)^2} \Rightarrow \alpha_{\perp} \approx \alpha^{1/3}, \quad (39)$$

where we have kept the single real root of the cubic equation and assumed $\alpha \ll 1$. This solution is consistent with the condition (27) provided α is bracketed as

$$x^3 \ll \alpha \ll 1. \quad (40)$$

In the relativistic regime, $\mathcal{A} = \mathcal{A}_{GR}$, we instead find

$$\alpha_{\perp} \approx \frac{\alpha}{x^2}. \quad (41)$$

together with the constraint $\alpha \ll x^3$ (which also guarantees that $\alpha_{\perp} \ll 1$).

Our main result (39) for the perpendicular viscosity is at odds with the result obtained in LP07. This is due to our inclusion of a damping term in the warp's equation of motion (18); the removal of that term (which to us appears unjustified) is equivalent to taking the limit $|\alpha_{\perp} - \alpha| \rightarrow \alpha$ in the formulae of the last three sections. In particular, (39) would be replaced by $\alpha_{\perp}/\alpha \approx 1/\alpha^2$ thus leading to the LP07 result $\alpha_{\perp} \approx 1/\alpha$. Putting aside the different functional form $\alpha_{\perp}(\alpha)$, it is clear that both models predict a dominant perpendicular viscosity, $\alpha_{\perp} \approx 0.5 - 10$ for the canonical value $\alpha \approx 0.1$. The relative ratio between the full prediction (22) and the Newtonian result, expression (39), is shown in Fig. 2 for a compact object at $x = 1/6$ and $q = 0.2$ (blue) or a less-compact system with $x = 1/20$ (red). Note that such a q value corresponds roughly to a spin frequency $\nu \sim 400$ Hz for a neutron star. At low values of the viscosity, we see significant departures: the ratio α_{\perp}/α is *lower* by a factor of ~ 10 for $\alpha \lesssim 10^{-2}$ for $x = 1/6$ and even still ~ 2 for $x = 1/20$. This implies that, generally speaking, we expect warped discs to be *less stable* when accounting for GR effects, as we explore next.

3.4 Hydrodynamical estimates for instability

Two effective viscosities, related to the drag coefficients λ and λ_{\perp} , have been introduced above. The formal analysis of Ogilvie (1999) reveals a third ought to be considered also, which includes contributions from radial stresses and encapsulates dispersive, wave-like torques which cause neighbouring rings of fluid to precess when misaligned (see equation 83 in Paris & Ogilvie 2018, for a definition). In this section, we

this is not a problem in this instance because we are considering the squared quantities. In later sections it will be important to keep track of the sign.

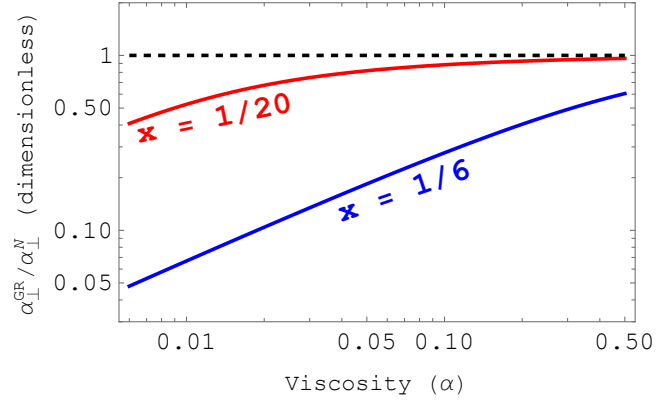


Figure 2. Ratio of the perpendicular viscosity coefficient, determined using the amplitude (22) and expression (38), to the Newtonian prediction (39) as a function of α for $q = 0.2$ and $x = 1/6$ (blue) or $x = 1/20$ (red). The horizontal line marks equality, reached after $\alpha \approx 0.1$ for the less compact case. Solutions asymptote to this value for large α .

examine how the adjusted amplitude (22) affects the stability of a disc using the hydrodynamic formalism introduced by Ogilvie (1999) and Doğan et al. (2018).

Adopting the notation of Doğan et al. (2018), the relevant hydrodynamical equations in an isothermal disc are that describing conservation of mass

$$\frac{\partial \Sigma}{\partial t} + \frac{1}{r} \frac{\partial}{\partial r} (r v \Sigma) = 0, \quad (42)$$

and angular momentum

$$\begin{aligned} 0 = & \frac{\partial}{\partial t} (\Sigma r^2 \Omega \ell) + \frac{1}{r} \frac{\partial}{\partial r} (\Sigma v_r r^3 \Omega \ell) \\ & - \frac{1}{r} \frac{\partial}{\partial r} (Q_1 \Sigma c_s^2 r^2 \ell) - \frac{1}{r} \frac{\partial}{\partial r} \left(Q_2 \Sigma c_s^2 r^3 \frac{\partial \ell}{\partial r} \right) \\ & - \frac{1}{r} \frac{\partial}{\partial r} \left(Q_3 \Sigma c_s^2 r^3 \ell \times \frac{\partial \ell}{\partial r} \right), \end{aligned} \quad (43)$$

respectively. The relevant viscosity coefficients have been rebranded as Q_i , related to ν and ν_{\perp} through $Q_1 = \nu \Omega'/c_s^2$ and $Q_2 = \nu_{\perp} \Omega/2c_s^2$ (Ogilvie & Latter 2013). By using the warp-free, thin-disc structure relations (1) within the definitions of Q_i yields the leading-order terms: calculating the higher-order corrections requires an analysis of the (GR) Navier-Stokes equations, beyond the scope of this article (see Ogilvie 1999, for a Newtonian analysis). It is easy, however, to show that the leading-order expressions for the two dissipative coefficients read (see equations 141–143 therein)

$$Q_1 \approx -\frac{3\alpha}{2} + \frac{\alpha_{\perp}}{8} |\psi_0|^2 + \mathcal{O}(|\psi|^4), \quad (44)$$

and

$$Q_2 \approx \frac{\alpha_{\perp}}{2} + \mathcal{O}(\psi^2), \quad (45)$$

applying to the case of a polytropic disk with adiabatic index $\Gamma = 5/3$. For the third coefficient, we adopt the result from Ogilvie (1999),

$$Q_3 \approx 3/8 + \mathcal{O}(|\psi|^2). \quad (46)$$

The stability problem now boils down to considering perturbations of the fluid (e.g., Σ) and warp (ψ_0) variables to

determine whether the eigenvalues of the perturbed variables indicate growth or damping. Skipping details which can be found in [Doğan et al. \(2018\)](#), linearisation of (43) eventually leads to the ‘coefficients determinant’ equation

$$\begin{vmatrix} s + 3\alpha - \frac{1}{4}\psi_0^2\alpha_{\perp} & -\frac{1}{2}|\psi_0|\alpha_{\perp} & 0 \\ 5\alpha\psi_0 - \frac{5}{12}(\psi_0^2 - 4)\alpha_{\perp} & s + \alpha_{\perp}(1 - \frac{1}{2}\psi_0^2) & -\frac{3}{8} \\ \frac{5}{8}|\psi_0| & \frac{3}{8} & s + \alpha_{\perp} \end{vmatrix} = 0, \quad (47)$$

where we have made use of Eqs. (44)–(46) (compare their equation 25). The eigenvalue $s = -i\omega/\Omega c_s^2 k^2$ is defined such that a positive real part of s indicates an unstable mode for wavenumber k . Eq. (47) reduces to a cubic in s , which can be solved easily given some relationship between α_{\perp} and α , yielding three solutions $s_i(\alpha, \psi)$. One may then check the maximum of the real parts of s_i to identify (in)stability.

Figure 3 shows the instability region as a function of viscosity (α) and warp ($|\psi_0|$) for a compact case with $x = 1/6$ and $q = 0.2$ as compared to the Newtonian limit ($x \rightarrow 0$). Even for these relatively extreme parameter choices, we see that the two regions largely overlap except at large warps where the scheme breaks down. In general though, GR terms make the system more unstable: for $\psi_0 \approx 1$, a viscosity of $\alpha \lesssim 0.06$ leads to instability in the GR case, while $\alpha \lesssim 0.09$ is needed for a Newtonian system. This occurs because the ratio α_{\perp}/α decreases when r_0 is small; see Fig. 2. For comparison, we also show the predicted instability window using the LP07 relation $\alpha_{\perp} = 1/\alpha$; the window is wider in this case. This is somewhat unintuitive since the value of α_{\perp} is typically greater in this case for small α , though occurs due to the opposing signs in the two terms within Q_1 (44). One can compare Fig. 3 directly with Figure 5 from [Doğan et al. \(2018\)](#), noting however that a numerical routine is used there to compute the Q_i as functions of α and ψ more accurately using the warped generalisation of the thin disc structure equations from [Ogilvie \(1999\)](#) and subsequent works.

4 INCLUSION OF A STAR-HOSTED MAGNETIC FIELD

In this section we reexamine various elements of the hydrodynamical case by including a magnetic field sourced by the central compact body. The resulting model will be one of a magnetoviscous disc. Where convenient, we adopt the notation $B_x = B/(10^x \text{ G})$ for the normalised magnetic field strength B .

4.1 Torque comparison

In the presence of a central body-hosted magnetic field, we expect the LT precession of adjacent fluid rings to be counteracted by a magnetic tension force due to the induced deformation in the field lines threading the disc. In order to scope out the parameter space where this effect could be important we repeat the back of the envelope calculation of Section 2.4 by including the magnetic field torque.

The total magnetic torque is given by

$$N_B \sim r^3 B_{\varphi} B_z, \quad (48)$$

which assumes an equatorial disc threaded by a vertical magnetic field that is azimuthally dragged by the rotational flow.

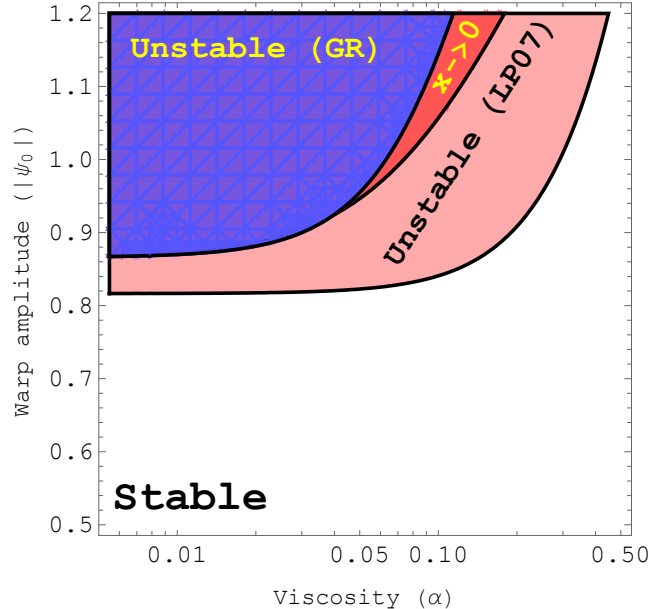


Figure 3. Stability diagram, as a function of viscosity and warp amplitude, for a highly-relativistic case with $x = 1/6$ and $q = 0.2$ (blue) and the Newtonian case ($x \rightarrow 0$; red). For comparison, we also show the prediction obtained when using $\alpha_{\perp} = 1/\alpha$ (pink) from [Lodato & Pringle \(2007\)](#). Shaded regions correspond to unstable cases with $\text{Re}(s) > 0$ from Eq. (47).

We have omitted a constant geometric prefactor so that we can use the same approximate expression for the component of \mathbf{N}_B along a given axis. For example, given the relative space orientation of the stellar magnetic and the disc, we expect the torque component perpendicular to the disc to be comparable in magnitude to the equatorial component.

For the precision of the present calculation it is sufficient to set $B_{\varphi} \sim B_z$ while the the poloidal field is assumed to be a dipole $B_z = -B_0(R/r)^3$ where B_0 is the field strength at the stellar surface (see [Glampedakis & Suvorov 2021](#), for a discussion). For the magnetic torque per unit mass, we find

$$T_B \sim \frac{B_0^2}{4\pi\rho} \frac{R^3}{r^3} \left(\frac{H}{r}\right)^{-1}. \quad (49)$$

Inserting the density profile (2) of a thin Keplerian disc, we can rewrite this as

$$T_B \sim \frac{3}{4} \frac{\alpha B_0^2}{\dot{M}} \left(\frac{H}{r}\right)^2 \frac{(GM)^{1/2} R^3}{r^{3/2}} \quad (50)$$

$$= \frac{9}{4} v_A^2 \frac{c^3}{GM} \left(\frac{H}{r}\right)^2 \frac{\alpha}{r^{3/2}}, \quad (51)$$

where $v_A^2 = B_0^2 R^3 / 3M$ is the volume-averaged stellar Alfvén speed. The magnetic field’s backreaction would be unable to prevent the LT precession of the disc and the ensuing tearing when

$$T_{\text{LT}} \gtrsim T_B. \quad (52)$$

This leads to the following ‘magnetic tearing radius’ condition

$$\bar{r}_{\text{t}} \lesssim \frac{q \sin \beta}{\alpha v_A^2} \frac{G \dot{M}}{c} \left(\frac{H}{r}\right)^{-2}. \quad (53)$$

Therefore, the magnetic field threading the disc suppresses

the onset of LT precession above some maximum distance r_t much alike the viscous forces, see Eq. (9).

We can obtain a more realistic result for the tearing radius by comparing the LT torque to the combined action of viscous and magnetic torques, i.e.

$$T_{\text{LT}} \gtrsim T_{\perp} + T_{\text{B}}. \quad (54)$$

Eq. (53) is now replaced by

$$2q \sin \beta \left(\frac{H}{r} \right)^{-2} \gtrsim \frac{9}{4} \frac{cv_{\text{A}}^2}{GM} \alpha \bar{r}^{1/2} + |\psi| \alpha_{\perp} \bar{r}^{3/2}, \quad (55)$$

with $|\psi| = \psi_0$. This is a cubic equation in $\bar{r}^{1/2}$ and can be solved analytically; the resulting roots, however, are unwieldy. It is far more informative to plot (55) (as an equation) in the B_0 - α plane for given values of the relevant stellar and accretion-specific parameters. For consistency however, this requires knowledge of how the $\alpha_{\perp}(\alpha)$ relation is modified by the magnetic field. Such a derivation is provided in Sec. 4.3, where we explore the inequality (55). In any case, the two terms on the right-hand side of expression (55) have a relative magnitude of

$$\left| \frac{cv_{\text{A}}^2 \alpha \bar{r}^{1/2} / GM}{\psi \alpha_{\perp} \bar{r}^{3/2}} \right| \approx 10^3 \left(\frac{B_0}{10^8 \text{ G}} \right)^2 \left(\frac{\alpha}{\alpha_{\perp}} \right) \left(\frac{R}{r_0} \right) \times \left(\frac{\dot{M}}{10^{-3} \dot{M}_{\text{edd}}} \right)^{-1} \left(\frac{0.3}{|\psi|} \right). \quad (56)$$

This shows that magnetic-adjustments to α_{\perp} itself are unlikely to play a significant role in tearing radii estimates, as the first term within (55) dominates except in systems with weak fields and large warps at large radii $r \gg R$. For weak fields, however, the non-magnetic estimate (38) for α_{\perp} may be applied reliably. Note that if the disc is truncated beyond the geodesic innermost stable orbit thanks to the magnetic field (i.e., at the Alfvén radius), one may expect that LT precession and disc-fragmentation would occur within the annulus $R_{\text{A}} \lesssim r \lesssim r_t$. For even larger fields, the magnetosphere may be completely truncated (see Section 7 in [Pastrouno, Haskell & Andersson 2017](#)).

4.2 Local analysis

Our next task is to include the magnetic field dynamics in the fluid parcel test-body model of the previous sections. The only modification required is the addition in the equation of motion of the Lorentz force density,

$$\mathbf{f}_{\text{L}} = \frac{1}{4\pi} [(\nabla \times \mathbf{B}) \times \mathbf{B}]. \quad (57)$$

To do so, we orient some local Cartesian coordinates so that $\hat{\mathbf{x}} = \hat{\mathbf{r}}$ and $\hat{\mathbf{y}} = \hat{\varphi}$ and assume a background magnetic field of the form

$$\mathbf{B}_0(x) = (0, B_y(x), B_z(x)), \quad (58)$$

which is trivially solenoidal. The motion of a fluid element off a circular equatorial orbit leads to the perturbed field

$$\mathbf{b}(t, x, z) = \mathbf{B} - \mathbf{B}_0 = (b_x, b_y, b_z). \quad (59)$$

For the background and perturbed Lorentz force we find, respectively,

$$(\mathbf{f}_{\text{L}})_0 = -\frac{1}{8\pi} \partial_x (\mathbf{B}_0^2) \hat{\mathbf{x}} = -\frac{1}{4\pi} (B_y B'_y + B_z B'_z) \hat{\mathbf{x}}, \quad (60)$$

and

$$\begin{aligned} \delta \mathbf{f}_{\text{L}} = \frac{1}{4\pi} \{ & [B_z(\partial_z b_x - \partial_x b_z) - (b_z B'_z + b_y B'_y) - B_y \partial_x b_y] \hat{\mathbf{x}} \\ & + (b_x B'_y + B_z \partial_z b_y) \hat{\mathbf{y}} + (b_x B'_z - B_y \partial_z b_y) \hat{\mathbf{z}} \}, \end{aligned} \quad (61)$$

where a prime denotes a d/dx derivative in this case.

The \mathbf{B} -field-augmented equations of motion are

$$\begin{aligned} \delta \ddot{r} + \Omega_r^2 \delta r + \lambda \delta \dot{r} = & H \Omega_0^2 \psi \\ & + \frac{1}{4\pi \rho} [B_z(\partial_z b_x - \partial_x b_z) - (b_z B'_z + b_y B'_y) - B_y \partial_x b_y], \end{aligned} \quad (62)$$

$$\ddot{\psi} + \Omega_{\theta}^2 \psi + \lambda_{\perp} \dot{\psi} = \frac{1}{4\pi \rho r_0} (b_x B'_z - B_y \partial_z b_y). \quad (63)$$

The evolution of the magnetic field itself is described by the induction equation,

$$\partial_t \mathbf{B} = \nabla \times (\mathbf{v} \times \mathbf{B}). \quad (64)$$

This is trivially solved by the background velocity, $\mathbf{v}_0 = v_0(x) \hat{\mathbf{y}}$, and \mathbf{B}_0 field; the perturbed equation is found to be

$$\begin{aligned} \partial_t \mathbf{b} = & (B_z \partial_z \delta v_x) \hat{\mathbf{x}} - \partial_x (B_z \delta v_x) \hat{\mathbf{z}} \\ & + [\partial_x (v_0 b_x - B_y \delta v_x) + v_0 \partial_z b_z - B_y \partial_z \delta v_z] \hat{\mathbf{y}}, \end{aligned} \quad (65)$$

where $\delta \mathbf{v} = (\delta v_x, 0, \delta v_z)$. Expanding its components and using $\nabla \cdot \mathbf{b} = 0$,

$$\partial_t b_x = B_z \partial_z \delta v_x, \quad (66)$$

$$\partial_t b_z = -B'_z \delta v_x - B_z \partial_x \delta v_x, \quad (67)$$

$$\partial_t b_y = v'_0 b_x - B'_y \delta v_x - B_y (\partial_x \delta v_x + \partial_z \delta v_z).$$

The first two expressions can be integrated in time and provides us with solutions for b_x, b_z which can be subsequently inserted in the previous equations of motion:

$$b_x = B_z \partial_z \delta r, \quad b_z = - (B'_z \delta r + B_z \partial_x \delta r). \quad (68)$$

The same procedure is not possible for b_y unless we are prepared to increase the differential order of the equations of motion. In order to avoid the overcomplication of what is supposed to be a toy model, we remove all b_y terms by setting $B_y = 0$ (i.e. we assume a *purely vertical* background magnetic field; see [Celora et al. 2025](#), for a discussion).

The resulting equations of motion are

$$\begin{aligned} \delta \ddot{r} + \left[\Omega_r^2 - \frac{B_z B''_z}{4\pi \rho} - \frac{(B'_z)^2}{4\pi \rho} \right] \delta r + \lambda \delta \dot{r} = & H \Omega_0^2 \psi \\ & + \frac{1}{4\pi \rho} [B_z^2 (\partial_z^2 \delta r + \partial_x^2 \delta r) + 3B'_z B_z \partial_x \delta r], \end{aligned} \quad (69)$$

$$\ddot{\psi} + \Omega_{\theta}^2 \psi + \lambda_{\perp} \dot{\psi} = \frac{B_z B'_z}{4\pi \rho r_0} \partial_z \delta r. \quad (70)$$

The test-body model of the present analysis means that we should collapse the derivatives as $\partial_z \approx 1/H, \partial_x = \partial_r \approx \psi_0/H$. This step, however, involves some loss of information related to the sign of each derivative. In order to keep track of these signs we introduce the bookkeeping parameters $\epsilon_i = \pm 1$ with $i = 1, 2, \dots$. We have the following algebraic expressions for the perturbed magnetic field:

$$b_x = \epsilon_1 \frac{B_z}{H} \delta r, \quad b_z = - \left(B'_z + \epsilon_2 B_z \frac{\psi_0}{H} \right) \delta r. \quad (71)$$

The equations of motion now take their final form

$$\delta\ddot{r} + \tilde{\Omega}_r^2\delta r + \lambda\delta\dot{r} = H\Omega_0^2\psi, \quad (72)$$

$$\ddot{\psi} + \Omega_\theta^2\psi + \lambda_\perp\dot{\psi} = \epsilon_4 \frac{B_z B'_z}{4\pi\rho H r_0} \delta r, \quad (73)$$

with

$$\begin{aligned} \tilde{\Omega}_r^2 &= \Omega_r^2 - \frac{1}{4\pi\rho} \left[(B'_z)^2 + B_z B''_z + \epsilon_1 \left(\frac{B_z}{H} \right)^2 \right. \\ &\quad \left. + \epsilon_2 \psi_0^2 \left(\frac{B_z}{H} \right)^2 + 3\epsilon_3 B_z B'_z \frac{\psi_0}{H} \right]. \end{aligned} \quad (74)$$

The key difference of this system compared to the one of Sec. 3 is that the magnetic field couples the two oscillators. Note that, modulo the magnetic shift of the orbital frequency, the radial equation is the same as in the non-magnetic model. The key difference appears in the vertical oscillator (73) which now contains a driving force term due to the magnetic coupling with the radial motion.

Our perturbative scheme requires $|\mathbf{b}| \ll B_0$ which means

$$|b_x/B_z| \ll 1, |b_z/B_z| \ll 1. \quad (75)$$

This, combined with the derivatives approximation, places an upper limit to the radial displacement

$$|\delta r| \ll \{r_0, H, H/\psi_0\} \Rightarrow |\delta r| \ll H. \quad (76)$$

We proceed to solve the system (72)-(73) by means of the normal-mode ansatz $\delta r = \mathcal{A}_r e^{i\sigma t}$, $\psi = \psi_0 e^{i\sigma t}$, with constant amplitudes \mathcal{A}_r and ψ_0 . The resulting algebraic system

$$(-\sigma^2 + \tilde{\Omega}_r^2 + i\sigma\lambda) \mathcal{A}_r = H\Omega_0^2\psi_0, \quad (77)$$

$$(-\sigma^2 + \Omega_\theta^2 + i\sigma\lambda_\perp) \psi_0 = \epsilon_4 \frac{B_z B'_z}{4\pi\rho H r_0} \mathcal{A}_r, \quad (78)$$

admits a non-trivial solution provided the determinant of the system's matrix vanishes, i.e.

$$(\sigma^2 - \tilde{\Omega}_r^2 - i\sigma\lambda)(\sigma^2 - \Omega_\theta^2 - i\sigma\lambda_\perp) = \epsilon_4 \frac{B_z B'_z}{4\pi\rho r_0} \Omega_0^2. \quad (79)$$

In the non-magnetic limit this equation returns the viscosity-modified orbital frequencies (plus viscous damping) of Section 3:

$$\sigma_r = i\lambda/2 \pm \omega_r = i\lambda/2 \pm (\Omega_r^2 - \lambda^2/4)^{1/2}, \quad (80)$$

$$\sigma_\theta = i\lambda_\perp/2 \pm \omega_\theta = i\lambda_\perp/2 \pm (\Omega_\theta^2 - \lambda_\perp^2/4)^{1/2}. \quad (81)$$

Recall that, in that earlier section, we only considered the σ_θ mode as the one driven by warp. In the present model, the coupling between the oscillators renders both modes relevant.

More interesting for the discussion of this section are the *magnetic field-dominated* modes. These modes, which we denote as σ_B , should appear when the viscosity terms in (79) are negligible compared to the magnetic terms. After setting $\lambda, \lambda_\perp \rightarrow 0$ we find the roots

$$\sigma_B^2 = \frac{1}{2} \left[\tilde{\Omega}_r^2 + \Omega_\theta^2 \pm \sqrt{(\tilde{\Omega}_r^2 - \Omega_\theta^2)^2 + \epsilon_4 \frac{B_z B'_z}{\pi\rho r_0} \Omega_0^2} \right]. \quad (82)$$

This result can be further expanded if we first define the disc's *local* Alfvén speed defined as

$$c_A^2 = \frac{B_z^2}{4\pi\rho}, \quad (83)$$

and subsequently rewrite (74) as

$$\begin{aligned} \tilde{\Omega}_r^2 &= \Omega_r^2 - \Omega_0^2 \gamma \left[\left(\frac{r_0 B'_z}{B_z} \right)^2 + \frac{r_0^2 B''_z}{B_z} + \epsilon_1 \left(\frac{r_0}{H} \right)^2 \right. \\ &\quad \left. + \epsilon_2 \psi_0^2 \left(\frac{r_0}{H} \right)^2 + 3\epsilon_3 \psi_0 \frac{r_0 B'_z}{B_z} \frac{r_0}{H} \right] \equiv \Omega_r^2 - \Omega_0^2 \tilde{\omega}_B, \end{aligned} \quad (84)$$

where we have defined the dimensionless parameters $\tilde{\omega}_B$ and

$$\gamma = \left(\frac{c_A}{r_0 \Omega} \right)^2. \quad (85)$$

With the help of the additional approximations from (26)

$$\Omega_r^2 - \Omega_\theta^2 \approx 6x\Omega_0^2, \quad \Omega_\theta \approx \Omega_0, \quad (86)$$

we find

$$\left(\frac{\sigma_B}{\Omega_0} \right)^2 = 1 + 3x - \frac{1}{2} \tilde{\omega}_B \pm \sqrt{\frac{1}{4} \tilde{\omega}_B^2 - 3x\tilde{\omega}_B + \epsilon_4 \gamma \frac{r_0 B'_z}{B_z}}. \quad (87)$$

The dominant term under the square root is the first one whenever $|\tilde{\omega}_B| \gg 1$. Given that $|r_0 B'_z/B_z| \sim 1$ this condition translates to $\gamma(r_0/H)^2 \gg 1$. After expanding the square root and dropping the relativistic terms we find

$$\left(\frac{\sigma_B}{\Omega_0} \right)^2 \approx 1 - \frac{1}{2} \tilde{\omega}_B \pm \frac{1}{2} \tilde{\omega}_B \pm \frac{\epsilon_4 \gamma}{\tilde{\omega}_B} \frac{r_0 B'_z}{B_z}, \quad (88)$$

where the sign choice in the last two terms is independent. Of particular interest is the (lower sign) mode

$$\sigma_B^2 \approx -\Omega_0^2 \tilde{\omega}_B \approx -\epsilon_1 \Omega_0^2 \gamma \left(\frac{r_0}{H} \right)^2 = -\epsilon_1 \left(\frac{c_A}{H} \right)^2, \quad (89)$$

which could signal the onset of an instability if $\epsilon_1 > 0$. In contrast, the upper sign choice leads to 'hydrodynamical modes'

$$\left(\frac{\sigma_B}{\Omega_0} \right)^2 \approx 1 \pm \frac{\epsilon_4 \gamma}{\tilde{\omega}_B} \frac{r_0 B'_z}{B_z}, \quad (90)$$

which are slightly modified by the magnetic field. Therefore, only expression (89) represents the magnetic-field dominated modes.

With the result (89) at hand, we can loop back to our previous discussion (see paragraph before Eq. 82) and quantify the necessary condition for the omission of the viscous terms. This is

$$|\sigma_B| \gg (\lambda, \lambda_\perp) \Rightarrow \frac{c_A}{H} = \gamma^{1/2} \frac{r_0}{H} \gg (\alpha, \alpha_\perp). \quad (91)$$

Combined with the condition $|\tilde{\omega}_B| \gg 1$ used earlier (and the standard assumption $\alpha \ll 1$) we can write the following 'global' condition for the emergence of the magnetic modes:

$$\gamma \left(\frac{r_0}{H} \right)^2 \gg (1, \alpha_\perp^2). \quad (92)$$

Note that γ is also a proxy for the ratio of magnetic to fluid energy density (or pressure) of the unperturbed disc; we must demand $c_A < v_\varphi$, otherwise the magnetic pressure would be strong enough as to cause the disruption of the disc. In par-

ticular, $\gamma = 1$ marks the location of the Alfvén radius³

$$R_A = \xi \frac{B_0^{4/7} R^{12/7}}{M^{2/7} (GM)^{1/7}}, \quad (93)$$

with⁴ $\xi \approx (3\alpha/4)^{2/7} (H/R_A)^{6/7}$ from Eq. (2). Based on this discussion we can easily obtain, for example, the radius at which $\gamma(r_0)(r_0/H)^n = 1$. This is equivalent to the Alfvén radius expression with a rescaled magnetic field $B_0 \rightarrow B_0(r_0/H)^{n/2}$, leading to $r_0 = R_A(R_A/H)^{2n/7}$. Therefore, the condition (92) is satisfied within the annular region

$$R_A \lesssim r_0 \ll R_A \left(\frac{R_A}{\alpha_\perp H} \right)^{4/7}. \quad (94)$$

This condition obviously implies an upper limit on the vertical viscosity, namely, $\alpha_\perp < R_A/H$.

The parameter γ clearly plays an important role in the dynamics of a magnetoviscous disc. Using the thin disc density profile (2) we can write it as

$$\gamma = \frac{3}{4} \frac{\alpha}{\dot{M}} \left(\frac{H}{r_0} \right)^3 \frac{B_0^2 R^6}{r_0^5 \Omega_0}. \quad (95)$$

The function $\gamma(r_0)$ is depicted in Fig. 4 for parameter choices appropriate for neutron star LMXBs (see also Sec. 5.3), together with a number of relevant radii and regions described in this section.

In the presence of both viscosity and magnetic field the full mode equation (79) must be solved. Ignoring the relativistic corrections in the frequencies, $\Omega_r \approx \Omega_\theta \approx \Omega_0$, we can write (79) in the following dimensionless form

$$(\tilde{\sigma}^2 - 1 + \tilde{\omega}_B - i\alpha\tilde{\sigma}) (\tilde{\sigma}^2 - 1 - i\alpha_\perp\tilde{\sigma}) = \epsilon_4 \gamma \left(\frac{r_0 B'_z}{B_z} \right), \quad (96)$$

where $\tilde{\sigma} = \sigma/\Omega_0$. This quartic equation can be solved analytically but the resulting expressions are too cumbersome. Nevertheless, the existence of unstable modes can be diagnosed by transforming $\tilde{\sigma} \rightarrow -i\zeta$ so that (96) becomes a fourth-order polynomial in ζ with real coefficients, from which the standard Routh-Hurwitz criteria apply for the existence of roots with negative real component (Anagnost & Desoer 1991). Noting the positivity and smallness of the viscosities, we expect that the Hurwitz criteria can be violated only if the constant term in the polynomial is negative. That is, if

$$\tilde{\omega}_B + \epsilon_4 \gamma \left(\frac{r_0 B'_z}{B_z} \right) > 1 \quad (97)$$

then there will exist an unstable branch. To leading order this reduces to the simple condition

$$\epsilon_1 \gamma (r_0/H)^2 > 1. \quad (98)$$

³ As we have seen, the presence of a warp ψ perturbs the magnetic field as $B_z \rightarrow B_z [1 + 2(\psi/H)\mathcal{A} \sin \omega_\theta t]$ which means that R_A should adjust accordingly. Such an oscillating field can lead to an effect known as ‘magnetic pumping’, accelerating particles reaching the Alfvén surface in a direction that depends on the phase of the oscillation (Kuijpers et al. 1997). Transient phenomena at frequencies of $\sim \omega_\theta$ with amplitudes depending on ψ/H would thus be expected, which could explain the \sim kHz quasi-periodic oscillations seen in a number of LMXBs (van der Klis 1998).

⁴ There is an inconsequential typo in expression (5) from Glampedakis & Suvorov (2021), where the Shakura & Sunyaev (1973) thin-disc ξ is reported with a slightly larger numerical prefactor. Note, however, that ξ is often treated as a free parameter.

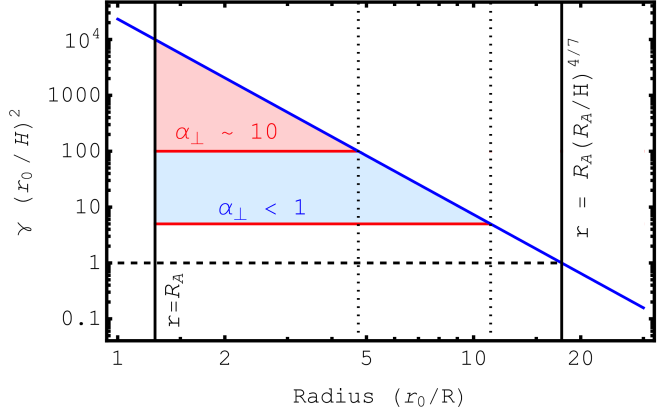


Figure 4. Dimensionless magnetic parameter $\gamma(r_0/H)^2$ from expression (95) as a function of radius for $H/r_0 = 10^{-2}$, $\alpha = 0.1$, $R = 10$ km, $M = 1.4M_\odot$, $B_0 = 2 \times 10^8$ G, and $\dot{M} = 10^{-6} M_{\text{Edd}}$ (solid blue curve). The solid, vertical lines depict the limiting values associated with total disc truncation ($\gamma = 1$; left) and equality in (94) (right) for $\alpha_\perp = 1$. The dotted, vertical lines mark the critical transition radius associated with the emergence of magnetic modes from condition (92) for either $\alpha_\perp \sim 1$ (with ‘ \gg ’ interpreted as five in this case; blue shaded region) or $\alpha_\perp \sim 10$ (red shaded region). The dashed, horizontal line marks $\gamma(r_0/H)^2 = 1$.

This can only hold for positive ϵ_1 in which case it is easy to see, using the structure equations (1), that it is equivalent to $c_A > c_s$. This inequality marks the onset of a magnetically-dominated regime with plasma $\beta_{\text{plasma}} < 1$.

The validity of condition (98) can be investigated numerically by simply computing the roots directly from Eq. (96) and checking if any satisfy $\text{Im}(\sigma) < 0$. The result is shown in Fig. 5 in the B_0 - α plane for some fiducial choices $\alpha_\perp = 10\alpha$ and $\dot{M} = 10^{-4} M_{\text{Edd}}$ at a radius of $r_0 = 5R$ for either unwarped ($\psi_0 = 0$) or highly-warped ($\psi_0 = 1$) cases. We see that the stability boundary for the numerical solutions trace a straight line corresponding to constant values of $B_0^2\alpha$. This follows from the combined proportionalities in $\rho \propto 1/\alpha$ and $c_A \propto B_0^2/\rho$, indicating the validity of inequality (98) as a diagnostic with small deviations provided by the warp parameter (at most a factor $\lesssim 2$ reduction to the critical B_0 for a given α). The fact that a magnetically-dominated transition corresponds precisely to the existence of unstable warp modes would appear to imply that episodic accretion is inevitable around stars with strong fields ($B_0 \gtrsim 10^9$ G) unless the disc is very inviscid ($\alpha \ll 10^{-2}$), as theoretically expected for ‘magnetically-arrested disks’ (Bisnovatyi-Kogan & Ruzmaikin 1976; Narayan, Igumenshchev & Abramowicz 2003). Whether a more realistic magnetic geometry involving a toroidal field would adjust this conclusion is unclear; such an extension, together with astrophysical implications, will be investigated elsewhere.

4.3 The $\alpha_\perp(\alpha)$ relation revisited

The next step of this analysis is the calculation of the velocities $\delta v_z \approx r_0 \dot{\psi}$, $\delta v_r = \delta \dot{r}$ and the use of the viscous dissipation balance (33) in order to arrive to a revised relation $\alpha_\perp(\alpha)$ for

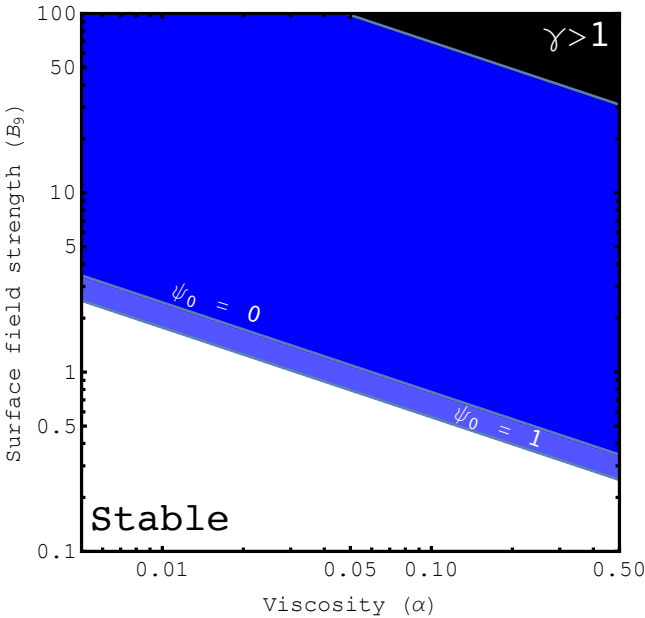


Figure 5. Stability diagram for $\alpha_{\perp} = 10\alpha$, $H/r = 10^{-2}$, and $\dot{M} = 10^{-4}\dot{M}_{\text{Edd}}$ at a radius of $r = 5R$ in the B_0 - α plane for unwarped ($\psi_0 = 0$; blue) or highly-warped ($\psi_0 = 1$; purple) cases. We fix $\epsilon_i = 1$ for all i . Shaded regions correspond to unstable cases with $\text{Im}(\sigma) < 0$. A visually-indistinguishable diagram is obtained for any choice $0.1 \lesssim \alpha_{\perp}/\alpha \lesssim 10$. The region shaded in black corresponds to $\gamma > 1$, where the scheme breaks down.

a warped magnetoviscous disc. From Eq. (77) we have

$$\mathcal{A} = |\mathcal{A}_r| = \frac{H\Omega_0^2\psi_0}{\sqrt{(\sigma_R^2 - \sigma_I^2 - \tilde{\Omega}_r^2 + \sigma_I\lambda)^2 + \sigma_R^2(2\sigma_I - \lambda)^2}}, \quad (99)$$

where σ_R/σ_I is a shorthand for the real/imaginary part of σ . For the non-magnetic modes (80)-(81) this expression returns the amplitude (22).

Using, as before, $\partial_r\delta v_z \approx \dot{\psi}$ and $\partial_z\delta v_r \approx \delta\dot{r}/H$, (33) yields

$$\frac{\alpha_{\perp}}{\alpha} \approx \left(\frac{\mathcal{A}}{\psi_0 H} \right)^2 = \frac{\Omega_0^4}{(\sigma_R^2 - \sigma_I^2 - \tilde{\Omega}_r^2 + \sigma_I\alpha\Omega_0)^2 + \sigma_R^2(2\sigma_I - \alpha\Omega_0)^2}. \quad (100)$$

This is an implicit expression for $\alpha_{\perp}(\alpha)$ because σ itself is, in general, a function of the alpha parameters. Ignoring relativistic corrections to the orbital frequencies, we can rewrite (100) as

$$\frac{\alpha_{\perp}}{\alpha} \approx \left[\left(\tilde{\sigma}_R^2 - 1 + \tilde{\omega}_B + \tilde{\sigma}_I(\alpha - \tilde{\sigma}_I) \right)^2 + \tilde{\sigma}_R^2(2\tilde{\sigma}_I - \alpha)^2 \right]^{-1}, \quad (101)$$

where, as before, we have normalised the frequencies as $\tilde{\sigma}_{R,I} = \sigma_{R,I}/\Omega_0$. These expressions clearly suggest that in the strong field regime of the disc (and especially in the vicinity of the Alfvén radius R_A) the presence of the magnetic field will significantly modify the simple $\alpha_{\perp}(\alpha)$ relations of Section 3.3.

The previously calculated inviscid magnetic modes σ_B are not suitable for a proper study of (101) as they cancel out to leading order with the $\tilde{\omega}_B$ term. The fact that the dispersion relation (79) and expression (100) (or 96 and 101) are coupled necessitates a simultaneous solution to determine both

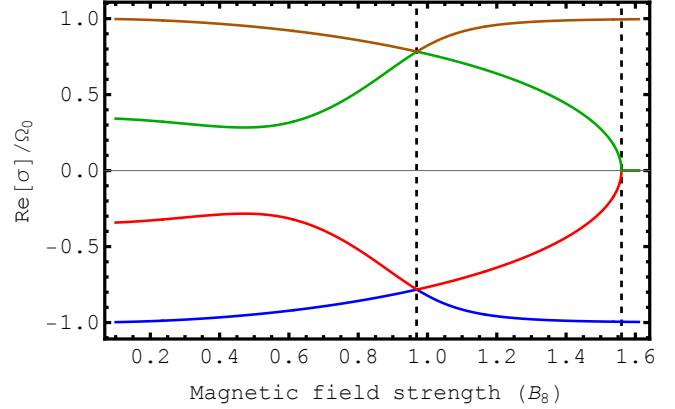


Figure 6. Real parts of normalised mode frequencies, $\tilde{\sigma}_R$, determined by solving equations (79) and (100) simultaneously as a function of $B_8 = B_0/10^8$ G, of which there are four in general (coloured curves). We fix $M = 1.4M_{\odot}$, $R = 10$ km, $M = 10^{-4}\dot{M}_{\text{Edd}}$, $\psi_0 = 0.3$, $H/r_0 = 10^{-2}$, $\alpha = 0.1$, and consider a radius $r_0 = 2R$ for demonstration. The solid, vertical lines mark the onset of avoiding crossings: tracing the colors (i.e., green to brown for $\tilde{\sigma}_R > 0$ or red to blue for $\tilde{\sigma}_R < 0$) illustrates the changing character where the derivative of the eigenfrequency with respect to B_0 flips sign. At high magnetic field strengths, two of the modes become imaginary and instead avoid a crossing in $\tilde{\sigma}_I$.

the mode frequencies and magnetically-augmented $\alpha_{\perp}(\alpha)$ relation in the general case. The problem is non-trivial however, as the modes exhibit avoided-crossings; this is shown in Fig. 6, depicting the real component $\tilde{\sigma}_R$, for some representative disc-star parameters. In this example, we see that already around $B_0 \approx 10^8$ G the two branches residing in the upper-half plane meet and subsequently swap character, with the same occurring for those in the lower plane. After this point, the branch of relevance concerns that which asymptotes to the magnetically-dominated case (88), so care must be taken as the crossing point varies as a function of radius for any given disc setup. Moreover, even before the transition point some mode frequencies become significantly affected by the magnetic pressure and increase in magnitude, highlighting the importance of magnetic corrections to the α_{\perp}/α relation. For example, at $B_0 \approx 10^8$ G we have that the lower-branches of $|\tilde{\sigma}_R|$ increase in frequency by a factor ≈ 2 relative to the non-magnetic limit. A second transition occurs at higher field strengths, where two of the modes become purely imaginary (around $B_0 \approx 1.5 \times 10^8$ G in this example).

Accounting for this phenomenon via a numerical routine that selects the magnetically-dominated branch after the transition point, the adjusted $\alpha_{\perp}(\alpha)$ relation is shown in Fig. 7 as a function of B_0 (top panel) or α (bottom).

When α is fixed, we normalise the result by the non-magnetic limit to show the convergent behaviour; as expected, for $B_0 \ll 10^8$ G the ratio is numerically indistinguishable from unity. As the field strength increases and $\tilde{\Omega}_r^2 - \Omega_r^2$ becomes large though we see a reduction in accord with expectations from the fact that large fields can make the system more unstable (Fig. 3). For example, at values of $\alpha \sim 10^{-2}$ we have $\alpha_{\perp}^B/\alpha_{\perp}^{B=0} \sim 10^{-3}$ for field strengths $B_0 \sim 10^9$ G – a value not atypical for mature neutron stars in tight binaries (e.g., Glampedakis & Suvorov 2021).

In the bottom panel, we instead plot the value of α_{\perp} di-

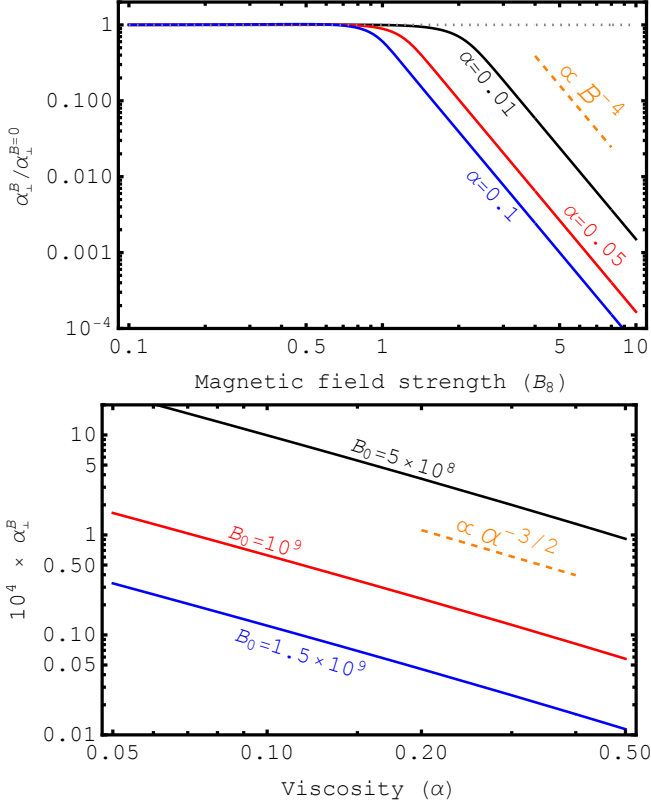


Figure 7. (Top panel): Ratio of the magnetically-adjusted perpendicular viscosity to the non-magnetic limit as a function of B_8 for a few representative values of α (solid curves). The dotted line marks unity, demonstrating convergence for weak fields. The dashed line depicts a B^{-4} falloff, which all cases succumb to after when B is large enough. (Bottom panel): Values of α_{\perp}^B for fixed field strengths (solid curves) as a function of α . The dashed line in this case depicts a $\alpha^{-3/2}$ falloff; clearly all cases follow this behaviour also, noting the strong fields chosen such that the magnetic branch resides within the entire parameter space shown. We set $H/r = 10^{-2}$, $\dot{M} = 10^{-4} \dot{M}_{\text{edd}}$, $R = 10^6$ cm, $M = 1.4M_{\odot}$, at a fixed radius $r_0 = 2R$.

rectly without normalising by the non-magnetic limit. This is done to illustrate the clear fall-off behaviour: when the field is sufficiently strong, such that the magnetically-dominated branch applies, we find $\alpha_{\perp}^B \propto 1/\alpha^{3/2}$. This indicates that strong magnetic fields, in addition to reducing the perpendicular viscosity like B^{-4} (top panel), lead to a further, indirect reduction as $\alpha \ll 1$ and the scaling departs significantly from the non-magnetic (39) and GR (41) cases. For canonical neutron-star like parameters, tiny values of $\alpha_{\perp}^B \lesssim 10^{-3}$ may be anticipated.

Taken together, the above numerical investigations suggest the following scaling in the magnetic field-dominated regime:

$$\left(\frac{\alpha_{\perp}}{\alpha}\right)_B \sim \frac{1}{\alpha^{5/2} \tilde{\omega}_B^2} \sim \frac{1}{\alpha^{5/2} B_0^4}, \quad (102)$$

where the appearance of $\tilde{\omega}_B$ is to be expected by its leading-order weight in the mode dispersion relation.

We can instead visualise the perpendicular viscosity in the B_0 - α plane more directly, as in Fig. 8, showing unnormalised values. Darker shades indicate smaller values. The region residing above in the solid curve corresponds to the regime where $\tilde{\Omega}_r^2 < 0$ and numerical treatments are strictly necessary as neither viscous nor magnetic terms are negligible.

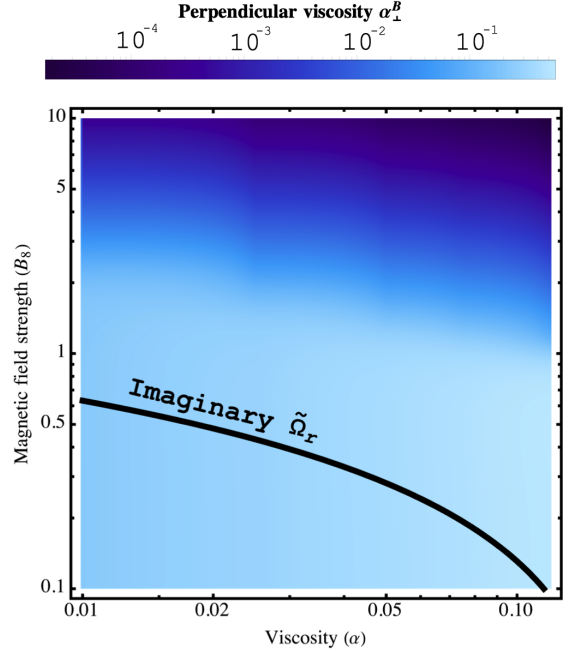


Figure 8. Similar to Fig. 7 but in the B_0 - α plane and for the *un-normalised* perpendicular viscosity. Darker shades indicate smaller values. The region residing above in the solid curve corresponds to the regime where $\tilde{\Omega}_r^2 < 0$ and numerical treatments are strictly necessary as neither viscous nor magnetic terms are negligible.

indicating a *reduction* as expected. This generally implies the disc is more prone to instabilities when strong fields are present as the vertical viscosity erodes. Moreover, we see a softer gradient in α_{\perp}^B as we increase α prior to the transition curve where $\tilde{\Omega}_r$ becomes imaginary from expression (74). In the neighbourhood of this curve, neither the inviscid or non-magnetic limits are valid: when $\tilde{\Omega}_r \sim 0$ we necessarily have $|\tilde{\Omega}_r|^2 \ll i\sigma\lambda$ within the dispersion relation (79). Even beyond this point, as σ is complex in general, one cannot naively discard viscous terms since the real and imaginary components do not exhibit a clear hierarchy.

4.4 The tearing radius revisited

We are now finally in a position to evaluate the tearing radius (55) with all ingredients included. One technical issue remains, which is that since γ depends on the *local* field strength (see Fig. 4) we must construct a three-dimensional table $\alpha_{\perp}(\alpha, B_0, r_0)$. This is needed because we do not know which radius applies *a priori*. This means that (55) is no longer a simple cubic with closed-form solutions at equality since α_{\perp} varies significantly with r_0 through B_z . We use a brute-force strategy to find the roots: first solve Eqs. (79) and (100) simultaneously over a fine grid of α, B_0 , and r_0 values with an inbuilt flag that locates the avoided crossing by comparing neighbouring eigenfrequencies ($\tilde{\sigma}_R$) and prints only values for α_{\perp} for the relevant branch. In practice, grids of size $96 \times 96 \times 52$ are used with log-spacing for $10^{-3} \leq \alpha \leq 0.1$, $10^7 \lesssim B_0/G \lesssim 10^{10}$ and $R \lesssim r_0 \lesssim 200R$. The full relation for α_{\perp} is constructed through linear interpolation, and then inserted into (55) to locate r_t via a Newton-Raphson method

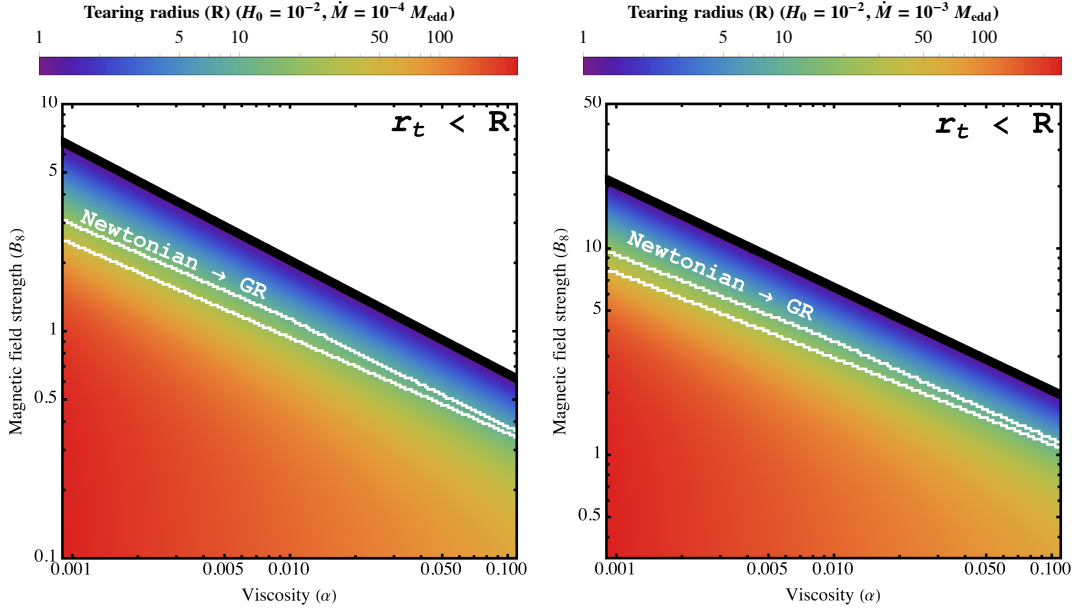


Figure 9. Tearing radii (r_t) in units of R , as a function of B_0 and α , for fixed parameter choices $M = 1.4M_\odot$, $R = 10$ km, $H/r_0 = 10^{-2}$, $q = 0.2$, and $\beta = |\psi| = 0.3$ for either $\dot{M} = 10^{-4}\dot{M}_{\text{edd}}$ (left) or $\dot{M} = 10^{-3}\dot{M}_{\text{edd}}$ (right). Above the respective white contours (with the lower and upper lines delimiting the range $|\alpha_\perp - \alpha| > 20$ and $|\alpha_\perp - \alpha| > 10$, respectively) one anticipates a transition to a relativistic regime, while above the black contour no solution exists as the tearing radius migrates beyond the stellar surface. Redder shades indicate greater values of r_t . Note the different vertical axis scaling between the two panels.

starting from the Newtonian guess (available as an analytic root when α_\perp is independent of radius).

Two such examples of carrying about the above are depicted in Fig. 9 with fixed values $M = 1.4M_\odot$, $R = 10^6$ cm, $H/r_0 = 10^{-2}$, $\beta = |\psi_0| = 0.3$, $q = 0.2$ but different accretion rates. The white contours within the panels depict the equalities $|\alpha_\perp - \alpha| = 20x$ (lower) or $|\alpha_\perp - \alpha| = 10x$ (upper), roughly delimiting the validity of the Newtonian regime: above this band one anticipates a transition towards intermediate cases where relativistic effects become important. As expected, this also corresponds to tearing radii close to the star (\gtrsim few stellar radii) where magnetic pressures are prominent.

That is, GR and magnetic effects tend to either be both important or unimportant, at least as far as how the $\alpha_\perp(\alpha)$ affects r_t is concerned. For higher accretion rates (right panel), we find an upward shift in the sense that greater values of the field strength and/or viscosity parameter are required to obtain the same tearing radius. This occurs as the magnetic torque (49) scales inversely with \dot{M} . Though not shown, disc thickness has a similar effect, in the sense that greater values of $H_0 = H/r$ lead to smaller tearing radii.

In any given model, as the field strength and viscosity increase, eventually the tearing radius reaches the stellar surface indicating no solution exists (shown by the thick, black line). For $\dot{M} = 10^{-4}\dot{M}_{\text{edd}}$, this occurs already for $B \lesssim 5 \times 10^8$ G at low viscosities ($\alpha \gtrsim 10^{-3}$). As anticipated from the ratio (56), a visually-indistinguishable figure is obtained if we were to use the non-magnetic $\alpha_\perp(\alpha)$ relation except at very low horizontal viscosities, α . In any case, a wide range of tearing radii $1 \lesssim r_t/R \lesssim 10^3$ could be accommodated in LMXB-like systems. Typically, the anticipated value reduces as the field increases (again highlighting the destabilising effect of central-body-hosted Lorentz forces).

5 ASTROPHYSICAL CONNECTIONS

In the preceding sections we examined the structure and instability thresholds for warped discs in cases where magnetic fields and LT torques are important. In this section, we apply the relevant expressions to some astrophysical systems. For instance, LMXBs host primaries which are rapidly rotating but weakly (relative to the neutron star population) magnetised (Sec. 5.3), while pulsations and cyclotron-line measurements from some ultra-luminous X-ray sources (ULXs) indicate they are slowly rotating but strongly magnetised (Sec. 5.4). Before moving to particular systems though, we outline some general considerations with respect to anticipated values of the [Shakura & Sunyaev \(1973\)](#) parameter (Sec. 5.1) and the dynamics of precessing rings (Sec. 5.2).

5.1 Anticipated values of α

A review from both the theoretical and observational points of view for what values α ought to take can be found in [King, Pringle & Livio \(2007\)](#). The basic conclusion reached there is that observations indicate typical values of $\alpha \sim \mathcal{O}(0.1)$, while numerical simulations find much smaller values (as low as $\alpha \sim 0.004$ in the 3D protoplanetary disc study of [Fromang & Nelson 2006](#), for instance).

Recent observational data from discs around compact objects suggest somewhat lower values for α . For LMXBs like Aql X-1 where the disc is illuminated by X-ray irradiation from inner regions, for instance, [Dubus, Hameury & Lasota \(2001\)](#) found that choosing $\alpha_h \sim 0.2$ in ‘hot’ (where hydrogen is ionized) or $\alpha_c \sim 0.03$ in ‘cold’ regions best reproduces the recurrence time of X-ray transients and associated light curves. As there are uncertainties pertaining to the conversion efficiency of rest-mass energy into radiation and other

systematics (e.g. hydrogen column density), different fits can be found in the literature. Recently, Coban & Ertan (2024) argued that $\alpha_h \sim 0.1$ together with $\alpha_c \sim 0.0075$ better match quiescent-state data for Aql X-1, with an even-lower $\alpha_c \sim 0.005$ during the source's outburst phase in 2010.

Values in the range $10^{-3} \lesssim \alpha \lesssim 10^{-1}$ could thus be considered ‘canonical’ for thin discs around neutron stars. In systems accreting in the neighbourhood of the Eddington rate, comparable values of $\alpha \sim 10^{-2}$ were estimated by Starling et al. (2004) using data from the Palomar-Green quasar sample (see their table 2) and Hameury & Lasota (2020) for the hyperluminous X-ray source HLX-1.

By contrast, advances in GRMHD modelling, which have permitted high-resolution capturing of shocks and the magnetorotational instability (MRI), skew towards *much larger* values: Liska et al. (2021, 2023) found $\alpha_{\text{eff}} \sim \mathcal{O}(10)$ in the inner regions of highly-tilted discs. Comparative values were recently found by Curd et al. (2025) using a different numerical code even for relatively low tilts ($\beta \lesssim 30^\circ$), which notably increases further for rapidly-rotating primaries (see their figure 7). These large values were at least partially attributed to the fact that warp-related shock dissipation – features that were difficult to capture in earlier studies – leads to huge increases in particle temperature and hence the effective viscosity. Lower values of α are found at larger radii where the disc has not been radiatively-thickened (see, e.g., figure 10 in Liska et al. 2023). In particular, in regions where the disc fragments due to thermal or hydrodynamic instabilities and the density plummets, values as low as $\alpha_{\text{eff}} \sim 10^{-2}$ were found by Liska et al. (2021). It should be noted that estimates of α in numerical studies are subject to some degree of definitional variation, as one must select a time band and average the velocity components to wash out oscillatory motions.

While a thorough survey of the literature lies beyond the scope of this paper, it is clear that there is some mismatch between the numerical and observational sectors. Importantly, the Shakura & Sunyaev (1973) parameter is not itself a direct measure of the isotropic viscosity appearing within Navier-Stokes equations, and thus it is not obvious that an *a priori* fixed functional form of the viscous stress-tensor ought to apply in astrophysical systems. This, together with the absence of shock modelling, could be (partially) responsible for such discrepancy between numerical and (semi-)analytic models.

The upshot is that in cold discs where *tearing* occurs – relevant for this paper – values of $\alpha_{\text{eff}} \sim \mathcal{O}(10^{-2})$ seem to be agreed upon in both the observational and theoretical sectors.

5.2 Masses and timescales for torn rings

Using the thin disc density profile (2), the amount of mass, ΔM , stored within some annulus $r_{\text{in}} \leq r \leq r_{\text{out}}$ is easily estimated as

$$\Delta M \approx 2\pi \int_{r_{\text{in}}}^{r_{\text{out}}} dr \int_0^{H(r)} dz r \rho(r) = \frac{4\dot{M} (r_{\text{out}}^{3/2} - r_{\text{in}}^{3/2})}{9H_0^2 \sqrt{GM\alpha}}. \quad (103)$$

If disc tearing occurs, we can identify ΔM with the mass stored within some precessing ring that eventually crashes into a neighbour and subsequently donates its material to the compact object. As discussed by Raj & Nixon (2021), the timescale over which angular momentum cancellation may be

expected is the differential nodal precession time

$$\tau_{\text{dnp}} = \frac{1}{\Omega_{\text{LT}}(r) - \Omega_{\text{LT}}(r + \Delta r)} \approx \frac{GM}{6c^3} \frac{r}{\Delta r} \frac{\bar{r}^3}{q}, \quad (104)$$

where Δr is the separation between the torn ring and its neighbours. In particular, it is reasonable to suppose that $\Delta r \approx H$ for strongly unstable rings, though it could plausibly be somewhat larger or smaller since the tearing process itself adjusts the hydromagnetic structure (e.g., the viscosity α ; see Liska et al. 2021). For a neutron star rotating with $q = 0.2$ (or $\nu \sim 400$ Hz), we estimate

$$\tau_{\text{dnp}} \approx 0.02 \text{ yr} \times \left(\frac{r}{10^8 \text{ cm}} \right)^3 \left(\frac{0.2}{q} \right) \left(\frac{10^{-3}}{H_0} \right) \left(\frac{1.4M_{\odot}}{M} \right)^2. \quad (105)$$

The further away the ring is from the star the longer the precession time, expected since the LT frequency decays with radius. On the other hand, the mass stored (103) also increases because the disc is thicker at larger radii (for constant H/r). Once the angular-momentum has been effectively cancelled it takes a further free-fall time for the material to land onto the stellar surface, though this is short relative to τ_{dnp} .

As a lower limit (in the context of accreting, magnetised neutron stars) we may expect that the inner radius is set by the Alfvén radius from expression (93),

$$\frac{R_A}{R} \approx 4.7 \left(\frac{\xi}{0.1} \right) \left(\frac{B_0}{10^9 \text{ G}} \right)^{4/7} \left(\frac{R}{10 \text{ km}} \right)^{3/7} \times \left(\frac{10^{-4} \dot{M}_{\text{edd}}}{\dot{M}} \right)^{2/7} \left(\frac{1.4M_{\odot}}{M} \right)^{1/7}. \quad (106)$$

The luminosity produced by the infalling ring mass can be estimated as

$$L_{\text{ring}} \sim \frac{GM}{R} \frac{\Delta M}{\tau_{\text{dnp}}}. \quad (107)$$

For a system with a ‘background’ luminosity (mostly emitted in the X-band for compact objects)

$$L_X \sim \frac{GM\dot{M}}{R}, \quad (108)$$

this represents a fractional luminosity increase of

$$\mathcal{L} = \frac{L_{\text{ring}}}{L_X} \sim \frac{\Delta M}{\dot{M}\tau_{\text{dnp}}}. \quad (109)$$

The ring’s outer radius may be set by the (magnetically adjusted) viscous tearing radius from Sec. 4.1, namely Eq. (55). Typical values of this tearing radius are shown in Fig. 9.

We now turn to estimating the relevant tearing masses (103) and torn-material accretion timescale (105) for several different astrophysical systems in the following sections.

5.3 Low-mass X-ray binaries

Even the most stable LMXBs containing a neutron star exhibit some degree of variability (Bahramian & Degenaar 2023). For example, observations of 4U 1543–624 taken in 2020 reveal that the 0.5–50 keV luminosity was a factor $\gtrsim 2$ weaker than of the peak luminosity during its 2017 brightening (Ludlam et al. 2021), while 4U 1705–44 (Muno, Remillard & Chakrabarty 2002) and MAXI J0556–332 (Page et al. 2022) have shown intermittent flux increases by factors of order ~ 10 from minimum to maximum over multi-year observational campaigns. Although the origin of large-amplitude

X-ray brightenings is not fully understood, such episodes are likely attributed to enhanced mass-accretion rates (see, e.g., [Ingram & van der Klis 2013](#)). Such episodes may be triggered by dynamical instabilities taking place in the disc owing to phenomena associated with the host star(s), such as from non-planar tides ([Larwood et al. 1996](#); [Doğan et al. 2015](#)), radiation-reaction due to illumination ([Pringle 1996](#); [Wijers & Pringle 1999](#)), or tearing ([Lodato & Price 2010](#); [Nixon & King 2012](#)). We consider the latter, especially supported in systems with ‘outburst’ recurrence times that show no evidence of periodicity ([Phillipson, Boyd & Smale 2018](#)).

As an example application of the formulae arrived at in Sec. 4, we focus on one of the more well-studied LMXBs, SAX J1808.4–3658 ([Wijnands & van der Klis 1998](#)). The object has an inferred field strength of order $B_0 \sim 2 \times 10^8$ G with a relatively low quiescent X-ray luminosity, $L_X \gtrsim 10^{32}$ erg/s ([Hartman et al. 2009](#)), similar to the parameters chosen in Fig. 4. As inferred from the standard relation (108), the system accretes (on average) at a rate well below the Eddington one, $\langle \dot{M} \rangle \sim 10^{-5} M_{\text{edd}}$. Moreover, the detection of a relativistically-broadened iron line from this source led [Papitto et al. \(2009\)](#) to infer that the inner edge of the accretion disc lies at $\approx 4.4^{+1.8}_{-1.4}$ Schwarzschild radii. This matches the Alfvén radius from expression (106) provided we have $\xi \lesssim 0.1$ (see also [Glampedakis & Suvorov 2021](#)).

In 2015, the object went into outburst, with the X-ray flux increasing by a factor ~ 60 for ~ 10 days (see figure 2 in [Sanna et al. 2017](#)). If the brightening were triggered by an episode of enhanced accretion from disc tearing, it would imply the following two conditions:

$$\mathcal{L}_{\text{J1808}} \approx 60, \quad \tau_{\text{dnp}}^{\text{J1808}} \sim 10 \text{ days}, \quad (110)$$

which follow from (109). From expression (105), we see that second condition within expression (110) is satisfied provided the tearing radius is $r_t \approx 115R$ (noting that SAX J1808.4–3658 has a spin frequency of $\nu = 400.98$ Hz).

Solving Eq. (55) in a manner similar to that carried out in Sec. 3 but instead allowing the disc thickness and viscosity to vary, it is easy to show that

$$H_0 \approx \frac{2\sqrt{2} \left(\sin \beta \dot{M} q \right)^{1/2} (GM)^{3/4}}{cr_t^{1/4} \left(3\alpha B_0^2 R^3 + 4\alpha_{\perp} c \dot{M} r_t |\psi| \right)^{1/2}}, \quad (111)$$

for given $r_t = r_{\text{out}}$. This implicit relation (noting that α_{\perp} depends on H_0 in the general, magnetoviscous case) is depicted in Fig. 10 for $\beta = |\psi| = 0.3$ as a demonstration. Fixing \dot{M} , B_0 , and r_{in} from the X-ray observations referenced above, r_t from the inferred precessional timescale in (110), and H_0 from expression (111) through the tearing-radius equation, all that remains free in the estimate for ΔM are the alpha parameters, the inclination, and the warp. However, unless α_{\perp} is of order unity for these parameters, it is the magnetic terms that are most relevant (see expression 56). In this limit, α drops out completely in the expression for ΔM and we find (noting $\sin \beta \sim \beta$ for small inclinations)

$$\Delta M_{\text{J1808}} \approx 2 \times 10^{-13} \left(\frac{\beta}{0.03} \right)^{-1} M_{\odot}. \quad (112)$$

While expression (112) may appear small, given the low quiescent accretion rate in SAX J1808.4–3658 we find that

$$\mathcal{L}_{\text{J1808}} \approx 47 \left(\frac{\beta}{0.03} \right)^{-1}, \quad (113)$$

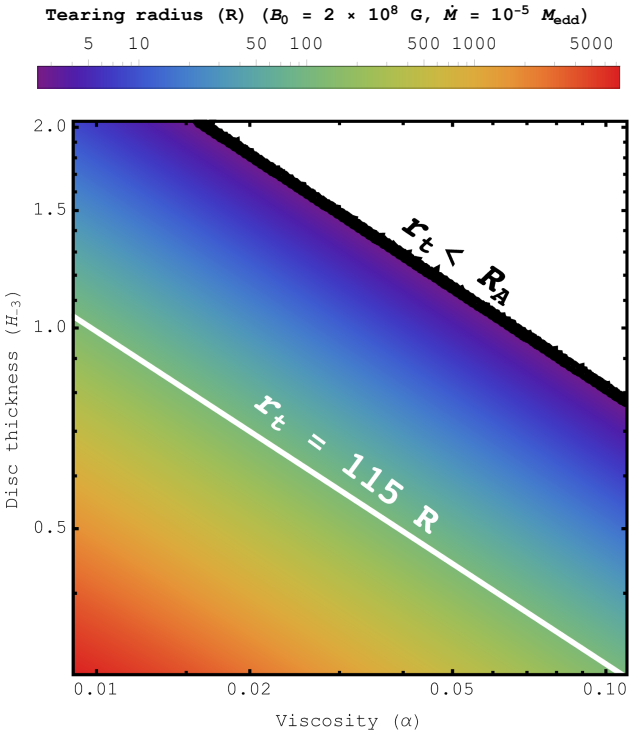


Figure 10. Tearing radius r_t in units of the stellar radius for parameters appropriate to SAX J1808.4–3658 (see text), as a function of viscosity and disc thickness (in units of $H_{-3} = 10^3 \times H/r_0$). The white contour corresponds to $r_t = 115R$, as anticipated from matching timescales within expressions (105) and (110), with the black line representing the inner radius of the disc as determined by [Papitto et al. \(2009\)](#).

which is comparable to the observed value (110). While not a direct measure of the *spin-orbit* misalignment, such a value of β is roughly consistent with the pulse-profile and hotspot modelling of [Ibragimov & Poutanen \(2009\)](#) who estimated the colatitude of the hotspot centroid to be between 4 and 10 degrees. If the neutron star mass and radius were larger than the ‘canonical’ values – which would decrease the inferred \dot{M} in quiescence – the estimate (113) increases further. We may therefore conclude that sensible parameters may explain the 2015 event via disc tearing.

Brighter events by contrast, such as that seen from Aql X-1 where the luminosity jumps by ~ 4 orders of magnitude over \sim month-long timescales ([Kocabiyik et al. 2025](#)), can only be explained for very low inclinations. This source has comparable quiescent X-ray luminosity and field strength estimates to SAX J1808, though spins faster ($\nu = 550.3$ Hz). We may thus expect $r_{\text{out}} \sim \text{few} \times 10^8$ cm by matching timescales using Eq. (105), giving

$$\mathcal{L}_{\text{Aql}} \sim 2 \times 10^2 \left(\frac{\beta}{10^{-2}} \right)^{-1}, \quad (114)$$

which cannot easily reproduce enhancements to the quiescent \dot{M} exceeding factors of $\sim 10^3$ for \sim months except for $\beta \ll 10^{-2}$. On the other hand, Aql X-1 exhibits a bimodal distribution of brightening episodes with approximately half being considerably dimmer ([Campana, Coti Zelati & D’Avanzo 2013](#)). In particular, the so-called ‘short-low’ category of

events lasting \sim days (Díaz Trigo et al. 2018) are readily explained by the tearing model as the ratio \mathcal{L} is large.

We close this section by remarking that given the largeness of the r_t values required to explain dramatic outbursts, the impact of magnetic and GR augmentations of the $\alpha_{\perp}(\alpha)$ relation are less relevant than changes to the r_t condition itself; see Eq. (55). However, many sources – most notably the class of transitional millisecond pulsars (tMSPs) – show X-ray variability even in quiescence on timescales as short as \lesssim minutes (see, e.g., Figure 2 in Baglio et al. 2023). Such unsteady flows could theoretically be explained by magnetic pumping, where the Alfvén radius oscillates due to the propagation of warp modes and triggers short-term variability (see Footnote 3). Modelling such flickering would certainly require the use of the adjusted viscosity relation since we anticipate $r_t \sim R_A$ from expression (105) (see also Fig. 8). Applications of the model developed here for the tMSP subclass of LMXBs will be explored elsewhere.

5.4 Ultra-luminous X-ray binaries

ULXs are an enigmatic class of exceptionally bright systems. While a number of these sources contain black holes, some of them show coherent pulsations – the so-called PULXs – and must therefore host neutron star primaries. As the name implies, these sources all show $\dot{M} > \dot{M}_{\text{edd}}$ in outburst but also spin slowly ($q \sim 10^{-4}$). PULXs thus reside in a different parameter space to LMXBs, altering the dynamical picture of the magnetoviscous disc and any would-be tearing.

While there is some debate in the literature, the expectation is that PULXs host magnetic field strengths of at least $B_0 \gtrsim 10^{12}$ G. For instance, a ~ 130 keV cyclotron resonance feature was observed in the spectrum of the Galactic PULX Swift J0243.6+6124, implying a magnetic field strength of $\gtrsim 10^{13}$ G near the surface (Kong et al. 2022).

Due to the combination of a strong field, large \dot{M} , and small q , we expect that disc tearing is unlikely to play a significant role in these systems. This is because the tearing radius (55) dips within the Alfvén sphere for realistic values of the disc thickness and viscosity, unless the field is dominated by higher multipoles due to magnetic burial or otherwise (Suvorov & Melatos 2019, 2020; Glampedakis & Suvorov 2021). Moreover, since the mass accretion rate is so high, one expects that the disc will be thickened by radiation pressures (White & Stella 1988; Chashkina, Abolmasov & Poutanen 2017) and thus the thin-disc model employed here may not apply in general.

Nevertheless, X-ray pulsations were discovered from Swift J0243.6+6124 even at luminosities of $L_X \sim 3 \times 10^{34}$ erg/s (Doroshenko, Tsygankov & Santangelo 2018), indicating a quiescent accretion rate as low as $\langle \dot{M} \rangle \sim 10^{-4} \dot{M}_{\text{edd}}$. Between 2017 and 2018, the object underwent a ‘giant outburst’ where the luminosity reached super-Eddington levels ($L_X \sim 2 \times 10^{39}$ erg/s; Wilson-Hodge et al. 2018; Tao et al. 2019). If we were to interpret this event via disc tearing we may write, similar to Eq. (110),

$$\mathcal{L}_{\text{J0243}} \sim 10^5, \quad \tau_{\text{dnp}}^{\text{J0243}} \sim 1 \text{ yr.} \quad (115)$$

Matching such values to the theoretical estimations is difficult even for extreme parameter choices. Fixing $q = 10^{-4}$, we get

from Eq. (105) that

$$r_{\text{out}} \sim 3 \times 10^7 (H_0/10^{-3})^{1/3} \text{ cm,} \quad (116)$$

in order to match timescales. Further taking a conservative $B_0 = 10^{12}$ G for the dipole component and $\xi = 10^{-2}$ to explain a compact magnetosphere (Doroshenko, Tsygankov & Santangelo 2018), matching expression (103) to that within (115) implies a tight relationship between H_0 and α . If $H_0 \approx 10^{-3}$ in line with standard assumptions, for instance, this demand amounts to an impossibly small $\alpha \sim 10^{-12}$.

Even ignoring the above, the tearing-radius solution to equation (55) cannot accommodate expression (116) for any reasonable range of H_0 and α . The problem becomes more severe if one uses larger values of B_0 , such as that inferred from quiescent spindown data (Serim et al. 2023), even if accounting for GR increases to the spindown luminosity (Stefanou, Suvorov & Pons 2025). For the less dramatic outburst from M82 X-2 around June 2015, where L_X was larger by a factor $\gtrsim 10^2$ compared to its quiescent return in June 2016 (Bachetti et al. 2020), it is still difficult to match data unlike in Aql X-1.

We conclude therefore that brightening episodes in PULXs are unlikely to be explained by tearing or that extra ingredients (e.g., a thick disc) are needed on the modelling side.

6 DISCUSSION

In this paper, we reexamine key assumptions considered in the literature used to estimate the perpendicular viscosity coefficient, α_{\perp} , in warped accretion discs and associated instability thresholds (Sec. 3). In addition, we incorporate GR effects and externally-sourced Lorentz forces at the level of a local fluid analysis (Sec. 4) semi-analytically for the first time (though see also Paris & Ogilvie 2018; Liska et al. 2021, 2023). Depending on the type of compact binary, either or both of these effects may be important and we find that the $\alpha_{\perp}-\alpha$ relationship can change dramatically; a summary of viscosity relations is given in Table 1. When the field becomes sufficiently intense (quantified by expression 91), we find that the classical warp modes transition into a magnetically-dominated family exhibiting avoided crossings (Fig. 6). On the physical side, the fact that α_{\perp} tends to decrease as a function of magnetic field strength (Figs. 7 and 8) implies that *tearing* is easier to achieve in general (quantified by Eq. 55 and Figs. 9 and 10). For compact binaries involving neutron stars, for example, this means that episodes of rapid mass infall triggered by warp instabilities appear as an even stronger candidate to explain outburst transitions (Sec. 5.3).

As in all studies of accreting compact objects, there are many parameters to consider. Most of these are unknown in general since they relate to microphysical interactions (e.g., the base viscosity α) or macrophysical orientation (e.g., the tilt angle β ; see Fig. 1). With respect to the latter, recent polarimetric instruments such as the Imaging X-ray Polarimetry Explorer (IXPE) are improving the prospects for estimating inclination angles in neutron-star X-ray binaries (Doroshenko et al. 2022; Kashyap et al. 2025). These data will be useful in future to more accurately assess the likelihood of tearing as an explanation for brightening episodes and hard-to-soft state transitions. The observation of linear X-ray polarisations at the level of a few percent in sources like Cygnus X-1

Table 1. Summary of key scaling relations between the vertical viscosity, α_{\perp} , to the horizontal viscosity, $\alpha \ll 1$, and other parameters (as defined in text) in a thin, warped disc.

Model	Relation	Reference
Newtonian, local (undamped)	$\alpha_{\perp} = 1/\alpha$	Lodato & Pringle (2007)
Newtonian, hydrodynamical	$\alpha_{\perp} \approx 1/2\alpha$	Papaloizou & Pringle (1983); Ogilvie (1999)
Newtonian, local (damped)	$\alpha_{\perp} \approx \alpha/(\alpha_{\perp} - \alpha)^2$	This work; Eq. (39)
GR-dominated, local	$\alpha_{\perp} \approx \alpha/x^2$	This work ($x^3 \ll \alpha \ll 1$); Eq. (41)
GR, local	Numerical from Eqs. (22) and (38)	This work ($B_0 = 0$); Fig. 2
Local, magnetically-dominated	$\alpha_{\perp} \propto \alpha^{-3/2} B_0^{-4}$	This work ($\gamma r_0^2/H^2 \gg 1$); Eq. (102) and Fig. 7
GR, local, magnetoviscous	Numerical from Eqs. (79) and (100)	This work; Fig. 8

(Krawczynski et al. 2022) could be interpreted via an edge-on viewing of a warped disc (Ingram et al. 2015), suggesting perhaps that tilt is common in Nature.

Aside from the LMXBs and ULXs considered in Sec. 5, warped disc phenomena could apply to other systems. One case concerns the elusive *quasi-periodic eruptions* (QPEs) seen in active galactic nuclei (AGN; Miniutti et al. 2019). A promising model of these events involves an unstable disc, where a strong magnetic field is invoked to fast-track the instability that leads to an eruption (Kaur, Stone & Gilbaum 2023). Since we find that warp instabilities set in precisely around the magnetically-dominated regime (see Fig. 5), discs in such a state could naturally experience tearing without any external (e.g. tidal) influence. Given the reduction of α_{\perp} as a function of B_0 (Tab. 1), it would be worth revisiting the viability of that scenario since we anticipate that the optical depth – controlling runaway heating events (Pan et al. 2022) – scales inversely with the viscosity (Shakura & Sunyaev 1973). As another example pertinent to AGN, data from the James Webb Space Telescope (JWST) are revealing a vast population of high-redshift galaxies that are extremely massive (Arrabal Haro et al. 2023; Lambrides et al. 2024). Their abundance poses a challenge for practically all cosmological evolution scenarios (De Luca et al. 2025); put simply, how is it possible for the black holes at the heart of these structures to grow so fast? If evidence is found for even moderately-strong magnetic fields in these systems, episodes of hyper-accretion would be easier to instigate.

Another case where the results obtained here may be relevant concerns the evolution of the recently-discovered ‘long-period transients’ (LPTs; Hurley-Walker et al. 2022). These sources pulse in the radio band in a manner remarkably similar to radio-loud magnetars, but with periods ranging from several minutes to hours. While their origin is unknown, the two leading models involve ‘spun-down’ magnetars (Cooper & Wadiasingh 2024; Suvorov, Dehman & Pons 2025a) or compact white-dwarf binaries (Qu & Zhang 2025; Suvorov, Dehman & Pons 2025b). In either case, supernova fallback or disc-fed accretion from a companion could play a role. Given that strong magnetic fields are required to produce coherent radio emissions, any would-be discs near such systems could be in the magnetically-dominated regime. In the binary picture, for example, the low duty cycle of many sources (such as GLEAM-X J 162759.5–523504.3; Hurley-Walker et al. 2022) could theoretically be explained by disc recession: warp-related instabilities deplete chunks of material such that magnetospheric interactions, otherwise impeded by the circling plasma, can take place to launch radio pulses.

Such events could be sporadic depending on the refilling time, explaining LPT irregularity. It would therefore be interesting in future to consider the tearing timescales described in Sec. 5 but for cataclysmic variables or polars rather than neutron stars or black holes.

ACKNOWLEDGEMENTS

We thank Suzan Doğan and Gordon Ogilvie for helpful correspondence on the nature of the Q_i coefficients and their computational routines. AGS is grateful for support provided by the Conselleria d’Educació, Cultura, Universitats i Ocupació de la Generalitat Valenciana through Prometeo Project CIPROM/2022/13 during the early stages of this work, the European Union’s Horizon MSCA-2022 research and innovation programme ‘EinsteinWaves’ under grant agreement No. 101131233, the Deutsche Forschungsgemeinschaft individual research grant 570901071, and the High Performance and Cloud Computing Group at the Zentrum für Datenverarbeitung of the University of Tübingen (Project ‘AnqaGW’).

DATA AVAILABILITY STATEMENT

Observational data used in this paper are quoted from the cited works. No new data were produced here. Computational routines are available on reasonable request.

REFERENCES

Anagnos J. J., Desoer C. A., 1991, Circuits Systems and Signal Processing, 10, 101
 Arrabal Haro P. et al., 2023, Nature, 622, 707
 Bachetti M. et al., 2020, ApJ, 891, 44
 Baglio M. C. et al., 2023, A&A, 677, A30
 Bahramian A., Degenaar N., 2023, in Handbook of X-ray and Gamma-ray Astrophysics, p. 120
 Balbus S. A., Hawley J. F., 1998, Reviews of Modern Physics, 70, 1
 Bardeen J. M., Petterson J. A., 1975, ApJL, 195, L65
 Bardeen J. M., Press W. H., Teukolsky S. A., 1972, ApJ, 178, 347
 Bisnovatyi-Kogan G. S., Ruzmaikin A. A., 1976, Ap&SS, 42, 401
 Brandenburg A., 2008, Physica Scripta Volume T, 130, 014016
 Campana S., Coti Zelati F., D’Avanzo P., 2013, MNRAS, 432, 1695
 Çoban Ö. F., Ertan Ü., 2024, ApJ, 961, 252
 Celora T., Palenzuela C., Viganò D., Aguilera-Miret R., 2025, arXiv e-prints, arXiv:2505.01208
 Chashkina A., Abolmasov P., Poutanen J., 2017, MNRAS, 470, 2799

Cooper A. J., Wadiasingh Z., 2024, MNRAS, 533, 2133

Curd B., Anantua R., West H., Duran J., 2025, MNRAS, 540, 1215

De Luca V., Del Grosso L., Franciolini G., Kritos K., Berti E., D’Orazio D., Silk J., 2025, arXiv e-prints, arXiv:2512.19666

Díaz Trigo M. et al., 2018, A&A, 616, A23

Doroshenko V. et al., 2022, Nature Astronomy, 6, 1433

Doroshenko V., Tsygankov S., Santangelo A., 2018, A&A, 613, A19

Doğan S., Nixon C., King A., Price D. J., 2015, MNRAS, 449, 1251

Doğan S., Nixon C. J., King A. R., Pringle J. E., 2018, MNRAS, 476, 1519

Dubus G., Hameury J. M., Lasota J. P., 2001, A&A, 373, 251

Fragile P. C., Liska M., 2025, in New Frontiers in GRMHD Simulations, Bambi C., Mizuno Y., Shashank S., Yuan F., eds., pp. 361–387

Fragile P. C., Mathews G. J., Wilson J. R., 2001, ApJ, 553, 955

Frank J., King A., Raine D., 1992, Accretion power in astrophysics., Vol. 21

Fromang S., Nelson R. P., 2006, A&A, 457, 343

Glampedakis K., Suvorov A. G., 2021, MNRAS, 508, 2399

Hameury J. M., Lasota J. P., 2020, A&A, 643, A171

Hartman J. M., Patruno A., Chakrabarty D., Markwardt C. B., Morgan E. H., van der Klis M., Wijnands R., 2009, ApJ, 702, 1673

Heinke C. O., Zheng J., Maccarone T. J., Degenaar N., Bahramian A., Sivakoff G. R., Toor S., 2025, The Astrophysical Journal Supplement, 279, 57

Herrnstein J. R., Greenhill L. J., Moran J. M., 1996, ApJL, 468, L17

Hurley-Walker N. et al., 2022, Nature, 601, 526

Ibragimov A., Poutanen J., 2009, MNRAS, 400, 492

Ingram A., Maccarone T. J., Poutanen J., Krawczynski H., 2015, ApJ, 807, 53

Ingram A., van der Klis M., 2013, MNRAS, 434, 1476

Kashyap U., Maccarone T. J., Pattie E. C., Ng M., Ravi S., Marshall H. L., 2025, ApJ, 992, 66

Kaur K., Stone N. C., Gilbaum S., 2023, MNRAS, 524, 1269

King A. R., Pringle J. E., Livio M., 2007, MNRAS, 376, 1740

Kocabiyik T., Güngör C., Sağlam M. T., Güver T., Bostancı Z. F., 2025, MNRAS, 537, 500

Kong L.-D. et al., 2022, ApJL, 933, L3

Krawczynski H. et al., 2022, Science, 378, 650

Kuijpers J., Fletcher L., Abada-Simon M., Horne K. D., Raadu M. A., Ramsay G., Steeghs D., 1997, A&A, 322, 242

Kumar S., Pringle J. E., 1985, MNRAS, 213, 435

Lambrides E. et al., 2024, arXiv e-prints, arXiv:2409.13047

Larwood J. D., Nelson R. P., Papaloizou J. C. B., Terquem C., 1996, MNRAS, 282, 597

Liska M., Hesp C., Tchekhovskoy A., Ingram A., van der Klis M., Markoff S. B., Van Moer M., 2021, MNRAS, 507, 983

Liska M. T. P., Kaaz N., Musoke G., Tchekhovskoy A., Porth O., 2023, ApJL, 944, L48

Lodato G., Price D. J., 2010, MNRAS, 405, 1212

Lodato G., Pringle J. E., 2007, MNRAS, 381, 1287

Ludlam R. M. et al., 2021, ApJ, 911, 123

Miniutti G. et al., 2019, Nature, 573, 381

Montgomery M. M., Martin E. L., 2010, ApJ, 722, 989

Muno M. P., Remillard R. A., Chakrabarty D., 2002, ApJL, 568, L35

Narayan R., Igumenshchev I. V., Abramowicz M. A., 2003, Publications of the Astronomical Society of Japan, 55, L69

Nealon R., Price D. J., Nixon C. J., 2015, MNRAS, 448, 1526

Nixon C., 2015, MNRAS, 450, 2459

Nixon C., King A., Price D., Frank J., 2012, ApJL, 757, L24

Nixon C. J., King A. R., 2012, MNRAS, 421, 1201

Ogilvie G. I., 1999, MNRAS, 304, 557

Ogilvie G. I., Latter H. N., 2013, MNRAS, 433, 2403

Page D., Homan J., Nava-Callejas M., Cavecchi Y., Beznogov M. V., Degenaar N., Wijnands R., Parikh A. S., 2022, ApJ, 933, 216

Pan X., Li S.-L., Cao X., Miniutti G., Gu M., 2022, ApJL, 928, L18

Papaloizou J. C. B., Pringle J. E., 1983, MNRAS, 202, 1181

Papaloizou J. C. B., Terquem C., 1995, MNRAS, 274, 987

Papitto A., Di Salvo T., D’Aì A., Iaria R., Burderi L., Riggio A., Menna M. T., Robba N. R., 2009, A&A, 493, L39

Pappas G., 2017, MNRAS, 466, 4381

Paris J. B., Ogilvie G. I., 2018, MNRAS, 477, 2406

Patruno A., Haskell B., Andersson N., 2017, ApJ, 850, 106

Phillipson R. A., Boyd P. T., Smale A. P., 2018, MNRAS, 477, 5220

Pringle J. E., 1992, MNRAS, 258, 811

Pringle J. E., 1996, MNRAS, 281, 357

Qu Y., Zhang B., 2025, ApJ, 981, 34

Raj A., Nixon C. J., 2021, ApJ, 909, 82

Raj A., Nixon C. J., Doğan S., 2021, ApJ, 909, 81

Sanna A. et al., 2017, MNRAS, 471, 463

Scheuer P. A. G., Feiler R., 1996, MNRAS, 282, 291

Serim M. M., Dönmez Ç. K., Serim D., Ducci L., Baykal A., Santangelo A., 2023, MNRAS, 522, 6115

Shakura N. I., Sunyaev R. A., 1973, A&A, 24, 337

Starling R. L. C., Siemiginowska A., Uttley P., Soria R., 2004, MNRAS, 347, 67

Stefanou P., Suvorov A. G., Pons J. A., 2025, MNRAS, 543, 273

Suvorov A. G., Dehman C., Pons J. A., 2025a, arXiv e-prints, arXiv:2505.05373

Suvorov A. G., Dehman C., Pons J. A., 2025b, ApJ, 991, 134

Suvorov A. G., Melatos A., 2019, MNRAS, 484, 1079

Suvorov A. G., Melatos A., 2020, MNRAS, 499, 3243

Tao L., Feng H., Zhang S., Bu Q., Zhang S., Qu J., Zhang Y., 2019, ApJ, 873, 19

Tremaine S., Davis S. W., 2014, MNRAS, 441, 1408

van der Klis M., 1998, Advances in Space Research, 22, 925

White N. E., Stella L., 1988, MNRAS, 231, 325

Wijers R. A. M. J., Pringle J. E., 1999, MNRAS, 308, 207

Wijnands R., van der Klis M., 1998, Nature, 394, 344

Wilson-Hodge C. A. et al., 2018, ApJ, 863, 9

APPENDIX A: THE ‘EXACT’ ORBITAL OSCILLATORS

This appendix provides a compact derivation of the equations of motion of a test body in a nearly circular/nearly equatorial orbit in the Kerr spacetime.

The textbook geodesic equations are (Bardeen, Press & Teukolsky 1972):

$$\Sigma^2 \dot{r}^2 = V_r(r) = [\mathcal{E}(r^2 + a^2) - a\mathcal{L}]^2 - \Delta [r^2 + (\mathcal{L} - a\mathcal{E})^2 + \mathcal{Q}], \quad (\text{A1})$$

$$\Sigma^2 \dot{\theta}^2 = V_\theta(\theta) = \mathcal{Q} - \cos^2 \theta \left[a^2(1 - \mathcal{E}^2) + \frac{\mathcal{L}^2}{\sin^2 \theta} \right], \quad (\text{A2})$$

$$\Sigma \dot{t} = V_t = \frac{r^2 + a^2}{\Delta} [\mathcal{E}(r^2 + a^2) - a\mathcal{L}] - a(a\mathcal{E} \sin^2 \theta - \mathcal{L}), \quad (\text{A3})$$

where $\Delta = r^2 - 2Mr + a^2$ and $\Sigma = r^2 + a^2 \cos^2 \theta$. The constants $\{\mathcal{E}, \mathcal{L}, \mathcal{Q}\}$ are per unit test body mass. We consider a nearly circular and nearly equatorial orbit, that is, the body’s radial and meridional position as a function of its proper time

τ , is described as

$$r(\tau) = r_0 + \delta r(\tau), \quad \theta(\tau) = \frac{\pi}{2} + \delta\theta(\tau). \quad (\text{A4})$$

The constant energy and angular momentum, $\mathcal{E}_0, \mathcal{L}_0$ of the circular orbit are determined by

$$V_r(r_0) = 0 = V'_r(r_0). \quad (\text{A5})$$

(For the same orbit the Carter constant is $\mathcal{Q}_0 = 0$.) Then, perturbing the above geodesic equations leads to the oscillator equations

$$\delta\ddot{r} + \bar{\Omega}_r^2 \delta r = 0, \quad \delta\ddot{\theta} + \bar{\Omega}_\theta^2 \delta\theta = 0, \quad (\text{A6})$$

with

$$\bar{\Omega}_{r/\theta}^2 = -\frac{V''_{r/\theta}}{2\Sigma^2} \Big|_{r=r_0, \theta=\pi/2}. \quad (\text{A7})$$

These are proper time frequencies; we can easily convert these expressions to coordinate time oscillators

$$\frac{d^2\delta r}{dt^2} + \Omega_r^2 \delta r = 0, \quad \frac{d^2\delta\theta}{dt^2} + \Omega_\theta^2 \delta\theta = 0, \quad (\text{A8})$$

with

$$\Omega_{r/\theta} = \frac{\bar{\Omega}_{r/\theta}}{t} = \frac{1}{\sqrt{2}V_t} (-V''_{r/\theta})^{1/2} \Big|_{r=r_0, \theta=\pi/2}. \quad (\text{A9})$$

In terms of the dimensionless parameters $q = a/M, x = M/r_0$ we find

$$\Omega_r^2 = \frac{x^3 - 6x^4 + 8qx^{9/2} - 3q^2x^5}{(1 + qx^{3/2})^2}, \quad (\text{A10})$$

$$\Omega_\theta^2 = \frac{x^3 - 4qx^{9/2} + 3q^2x^5}{(1 + qx^{3/2})^2}. \quad (\text{A11})$$